YALE
PEABODY
MUSEUM

JOURNAL OF MARINE RESEARCH

The *Journal of Marine Research,* one of the oldest journals in American marine science, published important peer-reviewed original research on a broad array of topics in physical, biological, and chemical oceanography vital to the academic oceanographic community in the long and rich tradition of the Sears Foundation for Marine Research at Yale University.

An archive of all issues from 1937 to 2021 (Volume 1–79) are available through EliScholar, a digital platform for scholarly publishing provided by Yale University Library at https://elischolar.library.yale.edu/.

Requests for permission to clear rights for use of this content should be directed to the authors, their estates, or other representatives. The *Journal of Marine Research* has no contact information beyond the affiliations listed in the published articles. We ask that you provide attribution to the *Journal of Marine Research.*

Yale University provides access to these materials for educational and research purposes only. Copyright or other proprietary rights to content contained in this document may be held by individuals or entities other than, or in addition to, Yale University. You are solely responsible for determining the ownership of the copyright, and for obtaining permission for your intended use. Yale University makes no warranty that your distribution, reproduction, or other use of these materials will not infringe the rights of third parties.

Barotropic, wind-driven circulation in a small basin

by S. P. Meacham[1] and P. S. Berloff[1]

ABSTRACT

We study the asymptotic behavior (large time) of a simple, wind-driven, barotropic ocean model, described by a nonlinear partial differential equation with two spatial dimensions. Considered as a dynamical system, this model has an infinite-dimensional phase space. After discretization, the equivalent numerical model has a phase space of finite but large dimension. We find that for a considerable range of friction, the asymptotic states are low-dimensional attractors. We describe the changes in the structure of these asymptotic attractors as a function of the eddy viscosity of the model. A variety of different types of attractor are seen, with chaotic attractors predominating at higher Reynolds numbers. As the Reynolds number is increased, we observe a slow increase in the dimension of the chaotic attractors. Using an energy analysis, we examine the nature of the instability responsible for the Hopf bifurcation that initiates the transition from asymptotically steady states to time-dependent states.

1. Introduction

In this paper, we revisit a central problem in oceanography: the way in which the wind drives the flow in an ocean basin as exemplified by a wind-driven barotropic circulation in a rectangular basin. The basic theory of this phenomenon is now a subject covered in most dynamical oceanography curricula, yet many aspects of the dynamics of the barotropic circulation remain to be clarified and these dynamics are currently an active area of research (e.g. Ierley, 1987; Cessi *et al.,* 1990; Cessi and Ierley, 1995; Ierley and Sheremet, 1995; Jiang *et al.,* 1995; Speich *et al.,* 1995; Kamenkovich *et al.,* 1995; Sheremet *et al.,* 1995). Here we explore some of the possible time-dependent solutions of a barotropic circulation problem, exposing, in the process, the existence, for identical values of the control parameters, of multiple dynamical regimes, a result that is foreshadowed by the existence of multiple steady solutions noted by Ierley and Sheremet (1995), Cessi and Ierley (1995) and Speich *et al.* (1995).

The wind-driven circulations in "small" and "large" basins have different stability properties (Meacham and Berloff, 1997). In basins with a sufficiently large meridional extent, the onset of instability, as the Reynolds number is decreased, is associated with a western boundary current instabilty (WBCI) of the sort investigated by Ierley and Young (1991). When the meridional extent of the basin is too small, the preferred instability is

instead one associated with part of the flow lying downstream of the main recirculation gyre (an "interior instability" or II). Ierley and Young looked at the linear instability of an infinitely long Munk boundary layer flow and found that instability first occurred at a critical wavelength, λ_c of about $18.7\delta_M$ where δ_M is the dimensional Munk boundary layer thickness at the onset of instability for a given wind-stress curl. For a δ_M of 26 km, this wavelength is about 490 km. Meacham and Berloff (1997) found that, in basins with meridional extents less than about twice this scale, the interior instability was preferred. We therefore distinguish between large basins, those with meridional extents appreciably greater than $2\lambda_c$, and small basins, those with meridional extents smaller than $2\lambda_c$. This is a relative measure, since the stability threshold depends on the strength and geometry of the wind-stress curl, and the boundary is fuzzy. When the meridional extent is comparable to $2\lambda_c$, the onset of instability can be associated with either the WBCI or the II, depending on the strength of the forcing. The work described in this paper is motivated by the nature of flows in basins like the Black Sea and we therefore use a basin in the "small" regime.

It is widely accepted that the flow in most ocean basins is turbulent over a broad range of spatial scales. At scales larger than a few kilometers, the paradigm for this is geostrophic turbulence (Rhines, 1979). The turbulent nature of the wind-driven circulation in small basins is vividly demonstrated by satellite (Oguz *et al.,* 1992) and hydrographic (Oguz *et al.,* 1993, 1994) data from the Black Sea. Numerical simulations of the same basin show a rich field of mesoscale eddies (Fig. 1 and Meacham, 1997).

At first sight, this turbulent flow looks rather complicated. However, on closer examination some suggestion of structure can be detected. For example in both observations and numerical simulations of the Black Sea, there seem to be some preferred locations at which eddies form more often. Repetitive patterns can be seen in the life cycles of some of the eddies and in the larger scale organization of the basin-wide flow. A quasi-permanent, small, strong gyre persists in the southwest of the basin, though its position fluctuates.

A lack of predictability in certain types of deterministic systems was explicitly recognized by Lorenz (1963). He further provided an elegant model which served to demonstrate that some types of chaotic motion may also contain a geometric simplicity in the form of low-dimensional objects—fractal attractors—that the motion asymptotically approaches when viewed in a dynamical phase space.

Ruelle and Takens (1971a,b; 1976) made the suggestion that the transition to turbulence in some flows might be explicable in terms of the successive bifurcations of a relatively low-dimensional dynamical system. A number of people have speculated that certain types of apparently disordered flow might in fact be "organized" by being constrained to lie close to a low-dimensional manifold embedded in the much larger phase space of the system. Examples of this include turbulent Taylor-Couette flow (e.g. Brandstater and Swinney, 1987) and the chaotic regime of the Belousov-Zhaboutinski reaction (Hudson and Mankin, 1981; Simoyi *et al.,* 1982; Roux *et al.,* 1983) (an example of "chemical turbulence"). In both of these cases, investigators have found evidence of low-dimensional dynamics, including chaotic motion on a low-dimensional strange attractor, in laboratory

YEAR 33.455, LEVEL= 5
→ = 30cm/s
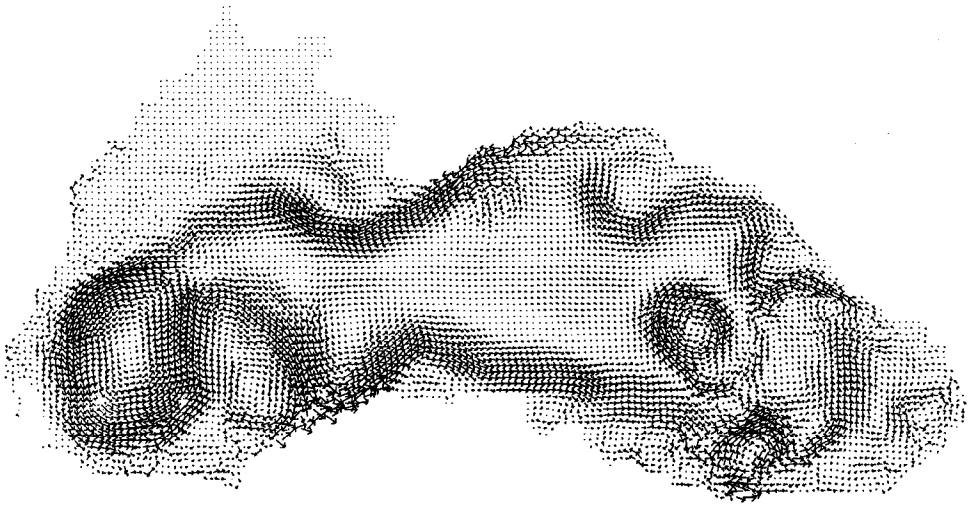
A: VELOCITY

Figure 1. Snapshot of a numerical simulation of flow in the Black Sea showing velocity vectors at 30 m. The model is based on the GFDL-MOM model with 20 levels in the vertical and is forced by seasonally varying wind stress and surface heat fluxes. Note the strong Rim Current, the strong southwestern recirculation and the many mesoscale eddies.

experiments. In several experiments with Rayleigh-Benard convection, Libchaber and his colleagues (e.g. Libchaber and Maurer, 1982; Libchaber *et al.,* 1982) have found a variety of bifurcations consonant with low-dimensional behavior.

   Rigorous proofs of the existence of low-dimensional asymptotic attractors for physical systems described by the Navier-Stokes equations are difficult to obtain and the few that exist assume rather restrictive conditions (e.g. Temam, 1995). Progress in this direction is reviewed by Robinson (1995). As far as the authors are aware, there is no formal proof that the steadily forced, dissipative barotropic flow problem in a rectangular basin approaches a finite-dimensional attractor. The work of Lions *et al.* (1992) goes a considerable way toward proving this for steadily forced flows governed by a version of the baroclinic primitive equations. Where formal bounds on attractor dimension can be obtained, they serve to prove the finite-dimensionality of the flow rather than to estimate the true dimension of the attractor. The formal bounds on attractor dimension tend to be very large. For example, Doering and Gibbon (1995) demonstrate that, in a periodic box, the upper bound on the dimension of the attractor for the two-dimensional Navier-Stokes equations is comparable, except for a logarithmic factor, to what one would estimate from taking the square of the ratio of the box-dimension to the dissipation scale. If this is applied to the circulation model that we discuss below, then, over the parameter range in which we find attractors with dimensions less than 3, the predicted upper bound is $O(10^4) - O(10^5)$.

The results cited in Robinson (1995), the experimental results of Brandstater *et al.* (1983), Brandstater and Swinney (1987), Simoyi *et al.* (1982), Roux *et al.* (1983) and many others, together with the work on the steady states of the barotropic circulation by Ierley and Sheremet (1995) and Cessi and Ierley (1995), all suggest that it may be possible to find finite-dimensional attractors of the barotropic circulation problem using an empirical approach. This is what we attempt here. A similar approach has been applied to geophysical problems by Ghil and his collaborators, e.g. Jiang *et al.* (1995), Speich *et al.* (1995).

In this study, we examine the behavior of a highly simplified numerical model of flow in a small basin. We adopt the paradigm of a complicated, autonomous, dynamical system with state X that evolves in time according to

$$\dot{X} = F(X; \boldsymbol{v}), \tag{1}$$

and with trajectories $X(t)$ that depend on the choice of initial condition $X(0)$ and a set of control parameters $\boldsymbol{v}$. In this study, the state vector, X, consists of the vorticity at all of the grid-points in a numerical model of the barotropic wind-forced circulation in a small basin and has a high dimension. The model contains a number of parameters; however, for much of this study, we fix all but one of them and vary only the value of the horizontal eddy viscosity v. Our objective will be to try to understand how the structure of the phase space of (1) varies as we change the control parameter v. In particular, we focus on how the natures of the attractors present in this phase space change as we vary v. Our purpose here is not to explore the sensitivity of the model to the strength of friction *per se* but to gain some idea of the range in Reynolds number over which the model manifests low-dimensional behavior and the nature of this behavior. An alternative way to modify the Reynolds number would be to modify the strength of the forcing, keeping friction fixed. This might be expected to produce similar though not identical results. (The strength of the wind stress and the strength of mixing do not enter the equations of motion in quite the same way so the results will not be the same but a similar increase in the strength and hence nonlinearity of the circulation can be achieved either by reducing the resistance to flow, for a given level of forcing, or by increasing the strength of the driving, for a fixed value of friction.)

Our expectation is that, for some range of Reynolds number, when the model is driven by a steady wind stress, the asymptotic state of the flow in this large-dimensional system may be determined by a limited number of low-dimensional attractors in the system's high-dimensional phase space. If these attractors have a fairly simple structure, they will correspond to a degree of organization in the observed physical flow and provide a simple way of representing the evolution of the flow, even when, physically, that flow looks rather complicated. At levels of friction low enough to be oceanographically relevant, we might anticipate that some of the asymptotic attractors of the system will be chaotic, nevertheless if their dimension is low, then the chaotic motion of the model is much simpler than would be the case if the probability density function of the turbulent flow were spread through a large-dimensional subspace of the high-dimensional phase space.

If a similar paradigm can be applied to the real ocean these ideas might be of use in constructing flow models with enhanced predictability (at least in a probabilistic sense). However, that is a rather ambitious leap. This paper is limited to statements about the behavior of general circulation models; the relation between GCMs and the real ocean is a much deeper topic.

When friction is sufficiently large, the response to steady forcing will be a steady circulation. When friction is sufficiently small, we anticipate a flow that exhibits spatio-temporal chaos. It is the path from the first to the second that we wish to explore and map out. Interesting points en route should be: the transition from steady to time-dependent flow, the onset of temporal chaos, and the transition to spatio-temporal chaos.

With these considerations in mind, the goals of this work can be summarized by the questions: when is the behavior of a large-dimensional ocean model dominated by low-dimensional dynamics? And, what is the nature of those dynamics? Only limited answers will be given here and only in the context of a single model.

Modeling wind-driven barotropic flow in a basin

In large ocean basins, a dominant feature of the upper ocean circulation is a strong, narrow current along the western boundary. Steady linear models of the wind-driven circulation, developed by Stommel (1948) and Munk (1950), were able to produce such a feature in the form of a frictional boundary layer. This layer allows the excess potential vorticity picked up by the fluid parcels as they move through the Sverdrup interior to diffuse into the boundary so that they can return to the interior of the circulation and repeat their progress around the basin. On a β-plane, linear frictional barotropic models of flows in rectangular basins with edges parallel to the geographical coordinate axes yield streamlines that are symmetric about the midlatitude line of the basin and consist of a single dominant cell, the center (i.e. the pressure extremum) of which lies to the west of the center of the basin. The flow along the western boundary is stronger than that along the eastern boundary, with the boundary layer character of the western boundary current increasing as friction is reduced. A second type of model of fundamental importance to circulation problems is the inertial circulation model of Fofonoff (1954). In this, forcing and dissipation are omitted while nonlinearity is retained. Several free solutions are possible, the simplest of which is a single cell that is symmetric about the midlongitude line of the basin and which has a center that is displaced toward the northern or southern edge of the basin depending on whether the cell is anticyclonic or cyclonic. Perturbing the linear viscous models with weak nonlinearity results in a meridional displacement of the center of the cell (Munk *et al.,* 1950) while perturbing the nonlinear model with friction moves the center of the basin-wide vortex westward. Thus in some sense the linear viscous models and the free nonlinear model of barotropic flow in a rectangular basin appear to lie at the ends of a continuum. The circulation in a real ocean is, of course, both unsteady and unsteadily forced, and is affected by both stratification and topography. However, if one were to smooth the forcing and construct a steady, flat-bottomed, barotropic model, that

included both frictional and inertial effects, then the parameters of the model would put it somewhere in the middle of this continuum. Following further work on the nature of nonlinear boundary layers by Charney (1955) and Morgan (1956), Moore (1963) proposed a rather elegant, steady barotropic model that included both frictional and inertial effects. In this model the northern and southern boundaries are not rigid but are assumed to coincide with latitude lines along which the wind stress curl goes to zero, and free slip boundary conditions are applied there. An asymptotic analysis yields a standing, spatially decaying Rossby wave in the region where the western boundary current leaves the western boundary and the flow returns to the interior of the domain. When the flow is strongly nonlinear, not all of the excess vorticity, picked up as fluid parcels move through the interior Sverdrup flow, can be removed as the parcels transit the western boundary current. Pedlosky (1987) suggests that the dynamical role of this standing Rossby wave is to provide the returning fluid parcels greater opportunity to diffuse their excess potential vorticity to the boundary of the domain so that they can reenter the interior circulation with potential vorticities appropriate to a (statistically) steady circulation. Il'in and Kamenkovitch (1964) showed that while a decaying Rossby wave can exist next to a free zonal boundary for a wide range of flow intensities, when the zonal boundary is rigid, the decaying Rossby wave can only exist when the flow is sufficiently weak. (For a discussion, see Cessi *et al.,* 1990 and Ierley, 1987.)

In the presence of a rigid zonal boundary, the need to dissipate more potential vorticity than a simple inertio-viscous boundary layer can handle leads to the formation of a recirculation gyre in the southwest corner of a cyclonic circulation (northwest for an anticyclonic circulation). This enhances the transport in the southern (northern) part of the western boundary layer and augments the destruction of excess potential vorticity there (Ierley, 1987; Cessi *et al.,* 1990). In the work we consider here, in which we treat a small basin, of a size roughly comparable to the Black Sea, with rigid boundaries, such a recirculation gyre will be a prominent feature.

Bryan (1963) made a numerical study of a barotropic circulation subject to slightly different boundary conditions than those used here. In it, he established the following general sequence, since confirmed by numerous other models.

— At low Reynolds numbers, the flow in the basin is weak, almost linear and steady. Streamlines are roughly symmetric about the midlatitude line of the basin. The meridional flow is intensified toward the western boundary.

— As the Reynolds number is increased, the asymptotic solution obtained by integrating from a resting ocean remains steady but is increasingly nonlinear in the western part of the basin where a prominent western boundary current forms. The interior of the basin has a Sverdrup-like flow. The north-south symmetry is lost and a nonlinear recirculating gyre begins to appear in the northwest corner of the basin. (Bryan's model is forced with an anticyclonic wind-stress.)

— Eventually a critical Reynolds number, R_c, is reached at which the asymptotic state ceases to be steady. The unsteady solution contains Rossby-wave-like features propagating westward from the eastern boundary.

Our initial goal in this paper is to understand a little more about the primary bifurcation in which the asymptotic state changes from a steady state to a time-dependent solution and then to explore the secondary bifurcations of the time-dependent asymptotic states.

2. Dynamical model

Our basic dynamical system is a finite-difference numerical model of wind-driven, barotropic flow in a small rectangular basin of uniform depth. Since we are not interested in resolving fast external gravity waves, we use a rigid-lid approximation. We will use no-slip boundary conditions. The governing equations describing the evolution of the zonal and meridional components of the velocity, (u, v) and the pressure, p are simply

$$u_t + uu_x + uu_y - fv = -p_x + \nu\nabla^2 u$$
$$v_t + uv_x + vv_y + fu = -p_y + \nu\nabla^2 v + \tau/H \qquad (2)$$
$$u_x + v_y = 0.$$

Here, we have absorbed the uniform fluid density into p and τ (the meridional wind stress), and assumed both a β-plane approximation, $f = f_0 + \beta y$, and uniformity of the kinematic viscosity ν. H is the (constant) fluid depth.

Using a potential vorticity/stream function formulation of the problem (e.g. Roache, 1982), Eq. (2) reduces to

$$\partial_t \nabla^2 \psi + J(\psi, \nabla^2 \psi) + \beta \psi_x = \nu\nabla^4 \psi + \text{curl}(\tau/H). \qquad (3)$$

(Note that we have treated the wind stress as a body force distributed throughout the depth of the fluid. The resulting vorticity equation differs slightly from that given by the quasi-geostrophic approximation. This difference lies in the form of the forcing term: $\text{curl}(\tau/H)$ here instead of the quasi-geostrophic $f\text{curl}(\tau/fH)$. The results of either model correspond to results that would be obtained for the other with a very slightly different wind-stress pattern. For the simple wind pattern used below, the qualitative differences in results are negligible.)

Letting L_x and L_y be the zonal and meridional dimensions of the basin, we limit our attention to a steady wind-stress of the form $\tau = (\tau_0/L_x)(x - L_x/2)$, which has a uniform, cyclonic curl. We wish to briefly use dimensional analysis to determine how many distinct parameters enter the problem. We first introduce the Munk boundary layer width, $l = (\nu/\beta)^{1/3}$, and then scale lengths with l, time with $(\beta l)^{-1}$, and stream function with βl^3. Eq. (3) becomes

$$\partial_t \nabla^2 \psi + J(\psi, \nabla^2 \psi) + \psi_x = \nabla^4 \psi + \epsilon \qquad (4)$$

where

$$\epsilon = \frac{l}{L_x} \frac{\tau_0}{\beta \nu H}.$$

Defining a Reynolds number, Re, a dimensionless basin width, γ^{-1}, and an inertial length scale, L, by

$$Re = \frac{\tau_0}{\beta \nu H}, \qquad \gamma = \frac{l}{L_x}, \qquad L = \frac{\beta \nu H L_x}{\tau_0},$$

we see that $\epsilon = Re\gamma = l/L$. The problem depends on three dimensionless parameters:

$$\epsilon = \frac{l}{L}, \qquad \gamma = \frac{l}{L_x}, \qquad \text{and } \delta = \frac{L_y}{L_x}.$$

The last two parameters, γ and δ, come from a consideration of the locations of the basin boundaries. δ is the aspect ratio of the basin. Together with the no-slip boundary conditions adopted here, and, in some cases, the choice of initial conditions, the specification of δ, ϵ and γ determines the flow field. (In a nondimensionalization of the equations of motion (2), a fourth parameter would appear, $B = f_0/\beta L_x$; however, this only affects the pressure distribution, not the flow or vorticity distribution, so it is dynamically irrelevant.)

For a given choice of basin geometry (i.e. δ), the problem has a two-dimensional parameter space (ϵ, γ). In Meacham and Berloff (1997), we explore the linear stability problem in more detail and map out the marginal curve in this parameter space for a variety of choices of aspect ratio. In this paper, we wish to exemplify the richness of the bifurcation structure of the barotropic circulation problem as the nonlinearity of the flow is increased. We therefore follow a single curve in the (ϵ, γ) plane that runs roughly normal to the marginal curve (both are shown in Fig. 2). This is achieved by using a dimensional, numerical version of (3), fixing the horizontal and vertical dimensions of the basin, and the strength of the wind stress, while varying the strength of the eddy viscosity, ν. For details of the linear problem, its dependence on both δ and the position along the marginal curve, and the nature of small amplitude nonlinear solutions near the marginal curve, the reader is referred to Meacham and Berloff (1997).

We record here the values of the various parameters that we will hold fixed:

$$L = 1024 \text{ km}, \qquad L_y = 512 \text{ km}, \qquad f_0 = 10^{-4} \text{s}^{-1}, \qquad \beta = 2 \times 10^{-11} \text{m}^{-1} \text{s}^{-1},$$

$$\frac{\tau_0}{\beta^2 L^3 H} = 2.3283 \times 10^{-8}.$$

The latter quantity corresponds to a southward wind stress of 0.05 Nm^{-2} at the western boundary of the basin and a northward wind stress of 0.05 Nm^{-2} at the eastern boundary. The size of the basin is comparable to that of the Black Sea. The main dimensional
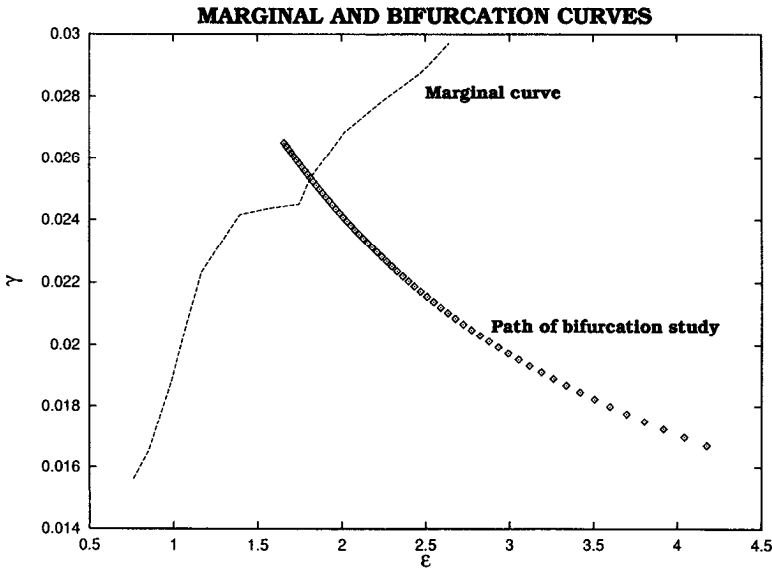
Figure 2. Parameter plane showing the marginal curve (dashed) and the curve along which the bifurcation sequence is developed (shown with diamonds).

parameter that we will vary is ν. We will concentrate on the range $100 \text{ m}^2 \text{ s}^{-1} < \nu < 400 \text{ m}^2 \text{ s}^{-1}$.

The numerical model of (3) is fairly standard. The equation is discretized on a 129×65 grid. An explicit time-stepping scheme is used for all terms in (3) (a second-order Runge-Kutta scheme with a time step of 1800s). The Poisson problem is solved using Hockney's FACR method (Hockney, 1970).

Considered as a dynamical system, the "variables" of the system consist of a value of $\nabla^2\psi$ at each of roughly 8000 nodes. This makes it a relatively large dynamical system.

3. Methodology

We made a number of calculations that differ by (i) the value of ν used and (ii) the initial condition. Each calculation furnishes one trajectory of the dynamical system in its natural (roughly 8000-dimensional) phase space. Since following the details of this is quite impractical, we chose a diagnostic that represents a spatial integral of the instantanteous state of the system and used the method of delay coordinates (Takens 1981; Packard *et al.*, 1980; Roux *et al.*, 1983) to reconstruct low-dimensional phase space approximations. The diagnostic that we used was the basin integral of the kinetic energy of the flow, $K(t)$.

a. Delay coordinates. An artificial phase space was constructed by defining a phase variable $x(t; \tau) \equiv (x_0, x_1, \ldots, x_{n-1})$ with

$$x_j = K(t - j\tau)$$

for a fixed delay τ.

The justification for this approach is provided by both embedding theorems and the empirical fact that it works! Whitney (1936) and Takens (1981) show that in general, an r-dimensional object can be embedded without self-intersection in an n-dimensional space provided that $n \geq 2r + 1$; however, simple r-dimensional objects can often be recognized in embedding spaces with $r < n < 2r + 1$, though they often exhibit self-intersection and so can look a little tangled, e.g. Roux *et al.* (1983) and Brandstater and Swinney (1987).

When the dynamics of the ocean circulation system are relatively simple (in particular, when they are confined to a low-dimensional subspace of the full phase space), the delay coordinates provided a straightforward picture of the behavior of the system. For example, steady states and periodic oscillations are readily picked out. In this way one can look for transitions (bifurcations) in the behavior of the system. In the event that the behavior of the system becomes chaotic, if the dynamics are such that the full system tends asymptotically to a strange attractor with a sufficiently simple structure, it may be possible to find a manifestation of this in the delay coordinate phase space for an appropriate choice of n. It is these kinds of behavior that we search for below. We will use the delay coordinates to attempt to construct a bifurcation sequence in the parameter ν and identify the changes in dynamical behavior that occur. We expect that if a low-dimensional strange attractor can be detected for some range of ν, then, as ν is decreased further, bifurcations in the structure of the attractor may eventually lead to a change from a low-dimensional attractor to a high dimensional attractor at which point our phase space reconstruction technique will fail.

The bifurcation thresholds are defined in terms of changes in the topology of the attractors and such changes are independent of the choice of the delay parameter τ. This allows a great deal of latitude in the choice of τ. The main criterion for picking τ is that the underlying dynamics should not be obscured. For example, if the motion is quasi-periodic with two dominant frequencies, ω_1 and ω_2, $\omega_2 < \omega_1$, then choosing τ larger than $2\pi/\omega_2$ will produce a very difficult to decipher phase space plot while choosing τ equal to one quarter of the faster period will generally expose a recognizable torus. A Poincaré section through this will then confirm the toroidal nature of the attractor. In the unsteady solutions below, the dominant fast frequency is always comparable to the frequency of the initial unstable mode so that a similar value of τ can be used throughout. For a more general time series that does not have a dominant peak in the high frequency part of its power spectrum, more formal choices of τ are the time to the first zero-crossing of the autocorrelation function or the time to the first minimum of the mutual information function (Fraser and Swinney, 1986). The choice of embedding dimension n is dictated by what can be represented on the page and so we use $n = 3$. This limits the type of attractor that can be recognized to fixed points, limit cycles and 2-tori, though, by using Poincaré sections, a strange attractor with a fractional dimension between two and three and a sufficiently simple structure can also be picked out.

b. Poincaré sections. Poincaré sections are a useful diagnostic tool that we will use later. In the work reported here, they are constructed as follows. We choose a fixed value of x_0, say C, and consider the plane with coordinates (x_1, x_2) given by $x_0 = C$. Choosing C so that the plane slices through the attractor of interest, we plot the points of intersection of the delay-coordinate phase space trajectory with this plane each time a trajectory passes through it, going from $x_0 < C$ to $x_0 > C$.

In the numerical experiments, the system was integrated from an initial condition either of rest or taken from a run made with other parameter values. The behavior reported is the asymptotic regime approached after some initial transient period (which varied in length between $O(10^3)$ and $O(10^4)$ days, in general), except where otherwise noted.

c. Spectral analysis. A complementary technique for studying the nature of attractors is the examination of the power spectrum of a time-series. Periodic solutions and period-doubling can readily be recognized by noting the changes in the distribution of isolated peaks, e.g. Libchaber and Maurer (1982) and Libchaber *et al.* (1982). In addition, toroidal attractors may be distinguished from chaotic attractors. Spectra of the former show discrete peaks with two or three (depending on the dimension of the torus) dominant peaks at incommensurate frequencies, together with smaller peaks produced by nonlinearity, and only a very low level of background noise. The spectra of chaotic attractors, while often still featuring some dominant spectral peaks, show a region of broadband noise.

4. Results

We describe a series of calculations in which each is distinguished by the value of ν used. To provide an overview, Figure 3 plots the values of ν used against "mean" energy observed. Figure 4 shows the periods of those solutions that were periodic, solutions that were either stationary or aperiodic are assigned a period of 0 in this figure. Most of our exploration has been confined to the range $100 \text{ m}^2 \text{ s}^{-1} \leq \nu \leq 400 \text{ m}^2 \text{ s}^{-1}$. For the size of basin and strength of forcing that we have used, the only aymptotic state, when $\nu = 400 \text{ m}^2 \text{ s}^{-1}$, appears to be a fixed point, corresponding to a steady circulation. At the other end of this range, $\nu = 100 \text{ m}^2 \text{ s}^{-1}$ is comparable to values of viscosity used in some ocean simulation studies but larger than those used in the better eddy resolving studies and larger than the estimates obtained from dye release experiments (e.g. from the NATRE experiment [Ledwell *et al.*, 1994]). Our main reason for stopping at $\nu = 100 \text{ m}^2 \text{ s}^{-1}$ is that regions of high dissipation in the flow become very narrow as ν is decreased and are poorly resolved in a model with 8 km resolution when $\nu < 100 \text{ m}^2 \text{ s}^{-1}$. Such structures play an important role in determining the flow patterns seen.

At large values of ν, the model quickly converges on a fixed point in the phase space and we see a steady circulation. On decreasing ν, an interesting sequence of attractors appears as one type of attractor successively loses stability to another. For a considerable range of ν, the dominant attractor is a low-dimensional object other than a fixed point. We have
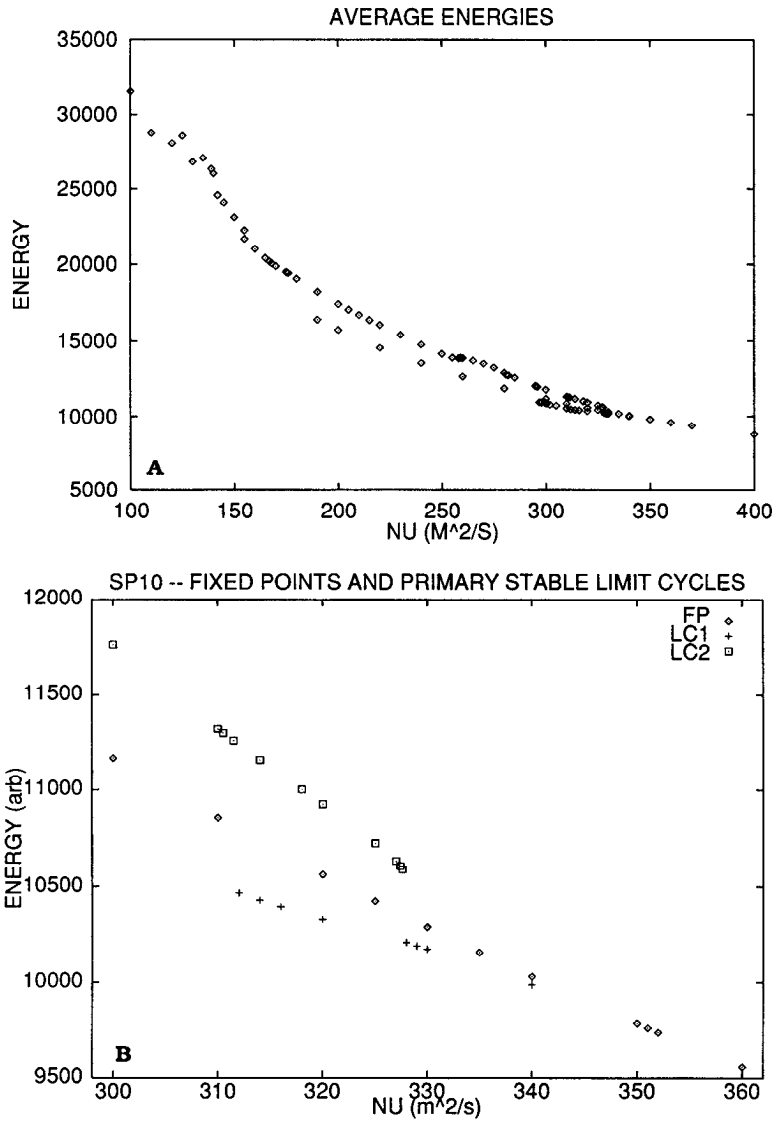
Figure 3. Energies of some of the asymptotic states observed at different values of the viscosity ν. (A) Various types of states over the range $100 \text{ m}^2 \text{ s}^{-1} < \nu < 400 \text{ m}^2 \text{ s}^{-1}$, (B) Energies of steady states (FP) and stable limit cycles (LC1, LC2) in the range $300 \text{ m}^2 \text{ s}^{-1} < \nu < 360 \text{ m}^2 \text{ s}^{-1}$.

observed the following (incomplete) types of behavior (indicated schematically in Figure 5 and described in more detail below) as ν is decreased: a limit cycle bifurcating supercritically from a fixed point solution, a limit cycle bifurcating subcritically from a fixed point solution, period doubling sequences, subharmonic resonances exemplified by quasi-periodic motion on attracting 2-tori and longer period phase-locked orbits, looped 2-tori

PERIODS OF LIMIT CYCLES
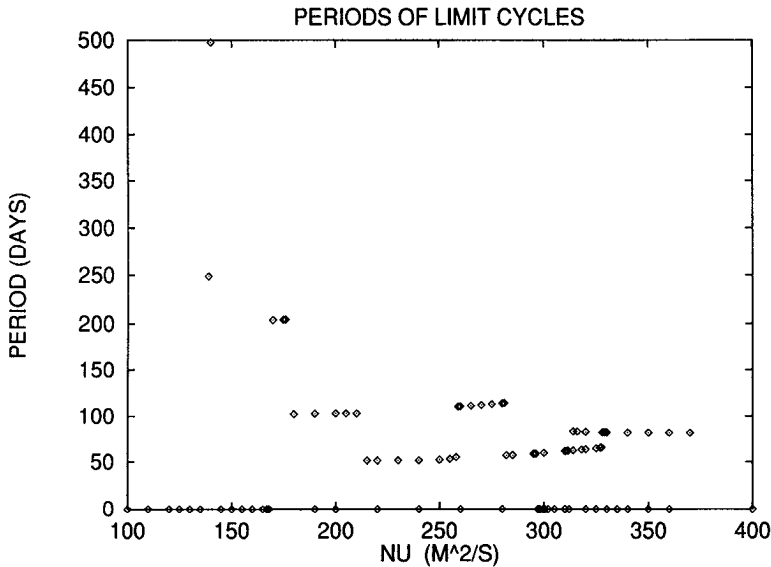
Figure 4. Periods (in days) of some of the limit cycle solutions found.

(subharmonic resonances involving a period-n orbit, where $n > 1$), and more complicated aperiodic motion. There appears to be at least two families of time-dependent solutions at moderate values of ν. Some of the more complicated aperiodic motion seen at lower values of ν may be the result of a collision between invariant sets from these two families.
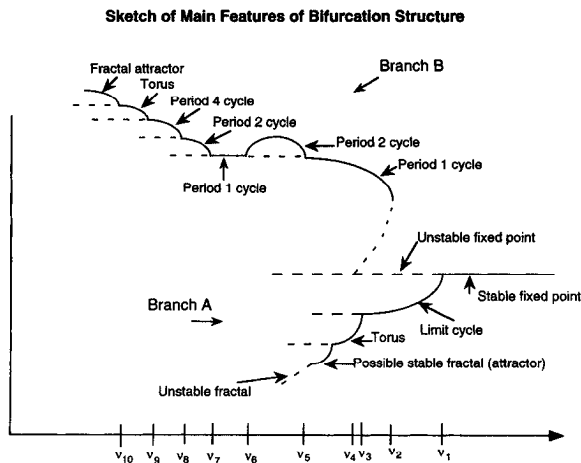

Figure 5. Sketch of the bifurcation structure found. The abscissa is ν, the ordinate is schematic. Only the most prominent bifurcations are shown and the values of ν indicated on the abscissa correspond to references in the text.

STEADY STREAMFUNCTION: NU=400M^2/S
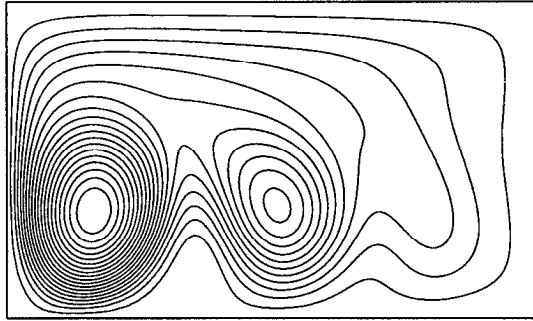
Figure 6. The pattern of flow in one of the steady state solutions as indicated by equally spaced stream function contours. This pattern is for $\nu = 400 \text{ m}^2 \text{ s}^{-1}$.

Overall, we have identified three families of solutions. These may be seen in Figure 3. One family is a family of fixed points, stable at sufficiently high ν but losing stability near $\nu = 350$. Lack of convergence in our steady state solver at low values of ν means that we are unable to continue following this branch of unstable solutions below $\nu = 190 \text{ m}^2 \text{ s}^{-1}$, though there seems no reason to believe that this branch of solutions does not continue. We cannot rule out the possibility that, in the vicinity of $\nu = 190 \text{ m}^2 \text{ s}^{-1}$, the branch of steady states curves back around to higher values of ν but we have not found any indication of this.

In the vicinity of $\nu = 350 \text{ m}^2 \text{ s}^{-1}$, the branch of fixed points undergoes a supercritical Hopf bifurcation, giving rise to a family of unsteady attractors that we can follow down to $\nu = 300 \text{ m}^2 \text{ s}^{-1}$. For values of ν close to 350, these take the form of stable limit cycles with periods on the order of 81 days.

A second family of unsteady solutions appears near $\nu = 327.6 \text{ m}^2 \text{ s}^{-1}$. This family of unsteady attractors can be traced to below $\nu = 100 \text{ m}^2 \text{ s}^{-1}$. The character of these families of solutions is described in more detail below.

a. Steady states. For sufficiently large values of ν, ($\nu > \nu_1$, where $\nu_1 \approx 350 \text{ m}^2 \text{ s}^{-1}$), the flow tends to a steady circulation. An example can be seen in Figure 6 which was obtained using $\nu = 400 \text{ m}^2 \text{ s}^{-1}$. A Sverdrup-like interior flow (predominantly northward in this problem) feeds a (southward) western boundary current. In the southwest corner, the boundary current turns eastward and feeds a steady meandering eastward jet pattern with a meander amplitude that decays to the east. Cyclonic recirculations are visible in the first two troughs of this wave. At lower viscosities, a cyclonic recirculation also appears in the third trough. The westernmost of these is the most prominent. For the particular values that we chose for the dimensional parameters, the maximum velocity of the western boundary current is of the order 40 cm s^{-1}. The energy of the steady states is plotted in Figure 7. This
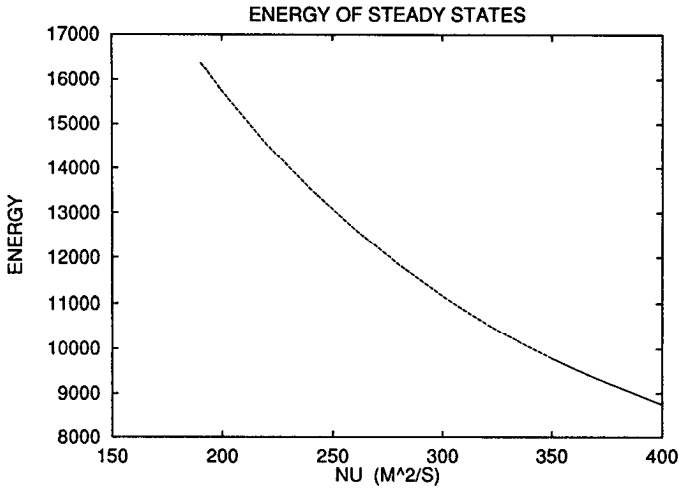
ENERGY OF STEADY STATES

Figure 7. A sketch of the variation of the total kinetic energy of the flow in the basin for the steady state solutions as a function of v. Both stable (solid curve) and unstable (dashed) states are shown. The units of energy are essentially arbitrary.

corresponds to one of the branches seen in Figure 3. As v decreases below 350 m^2 s^{-1} [v_1], the model, when started from an initial state of rest, becomes attracted to a limit cycle. However, by using an iterative scheme it is possible to still converge to a fixed point for a range of v below 350 m^2 s^{-1}, down to $v \approx 190$ m^2 s^{-1}. From their spatial structures and energies, these fixed points appear to be the continuation of the branch of fixed points seen for $v > 350$ [v_1]. The techniques that we use for finding steady states do not permit an exploration of the extent of the basins of attraction of the fixed points. It is known that, under some circumstances at least, wind-driven barotropic circulations in rectangular domains may exhibit multiple steady equilibria (Ierley and Sheremet, 1995; Cessi and Ierley, 1995), though whether multiple steady states exist depends on the model parameters. In this work, we searched for multiple steady states in $v > v_1$ but found only the single branch of steady states described above.

   If we make the assumption that the no-flow initial condition is not a special case, and that the approach to the stable fixed point is generic, then, by studying the way in which the fixed point is approached, we can estimate the dominant eigenvalue that would be obtained if we were to linearize the system about the fixed point. The approach to the fixed point is a flat (2-D) spiral so that the eigenvalues with the least negative real part must occur as a complex conjugate pair, $\lambda = -\sigma \pm \iota\omega$. The behavior of the dominant pair of eigenvalues as a function of v is shown in Figure 8. As $v \rightarrow v_1$, $\lambda \rightarrow 0 + \iota\omega_0$. As v crosses v_1, the obvious conclusion is that a supercritical Hopf bifurcation occurs (there is support for this in the next section). Below v_1, the fixed point still exists but is linearly unstable for those values of v at which we have checked stability.

REAL PART OF DOMINANT EIGENVALUE
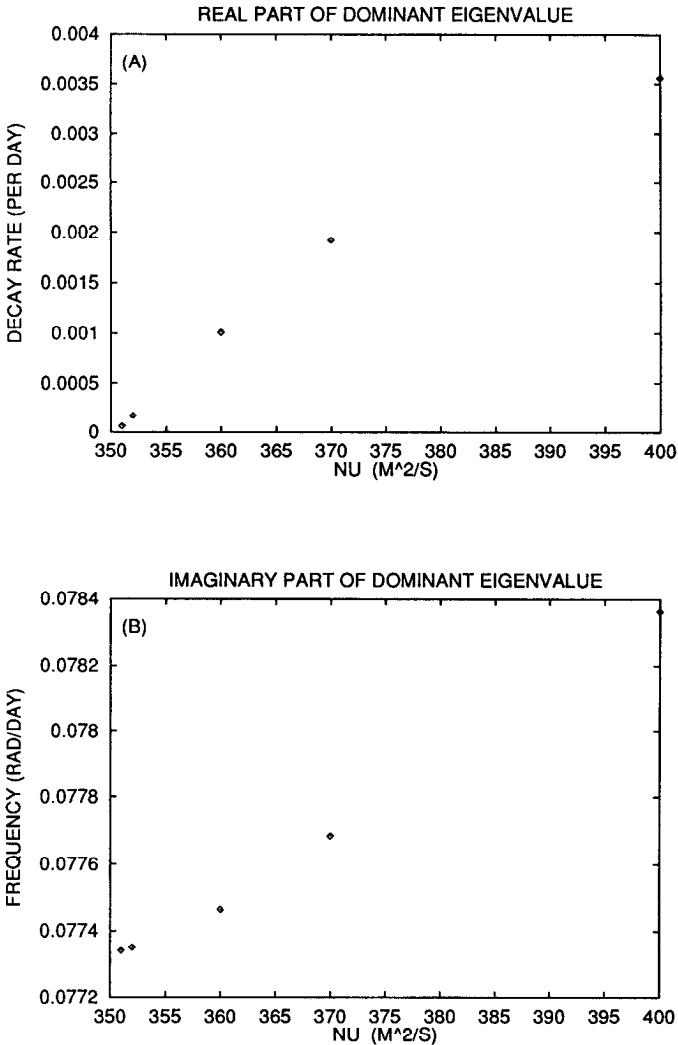

IMAGINARY PART OF DOMINANT EIGENVALUE

Figure 8. Real and imaginary parts (decay rate and frequency) of the most slowly decaying normal modes of the stable steady circulations for v near the marginal point, v_1. Note the linear behavior of the decay rate.

b. Periodic solutions. An example of a limit cycle may be seen in Figure 13a as a periodic trajectory in an artificial phase space constructed using delay coordinates (Takens, 1980; Packard *et al.*, 1980). The coordinates [$x(t)$, $y(t)$, $z(t)$] of a phase point in this space are constructed from the time-dependent, basin-integrated kinetic energy of the model, $K(t)$, using $x(t) = K(t)$, $y(t) = K(t - \tau)$, $z(t) = K(t - 2\tau)$, with $\tau = 16.667$ days.

The branch of unsteady, low-dimensional solutions, which starts as limit cycles spawned by the Hopf bifurcation at $v = v_1$, can be continued to lower values of viscosity. We will

call this set of solutions, branch A. At first, the solutions retain the form of limit cycles, down to a value of $v = v_3 \approx 311$ m^2 s^{-1}. For this range of v, the period, $T(v)$, amplitude, $A(v)$, and average energy, $E(v)$ of the limit cycles, plotted against v, may be seen in Figure 9. Here, A and E are defined in terms of the maximum and minimum energies encountered during the limit cycle; A is the difference of the maximum and minimum energies, while E is their arithmetic mean. For the purposes of comparison, we also include on Figure 9 information about some of the stable limit cycles associated with a second branch of time-dependent attractors and the period of the dominant (stable) eigenvalue of some of the steady states. At v_1, the period is approximately 81 days. As v is reduced, the period increases slightly so that by $v = 312$ m^2 s^{-1} it is 82.78 days. The amplitude increases with decreasing v. Figure 10 shows the circulation in the basin at a sequence of stages in the limit cycle for $v = 312$ m^2 s^{-1}.

This branch of unsteady solutions (branch A) can be continued below $v = 311$ m^2 s^{-1}, down to about $v = 300$ m^2 s^{-1}. This continuation is described in the next subsection. Below $v = v_2 \approx 327.6$ m^2 s^{-1}, a second branch (branch B) of unsteady solutions is encountered. The average energy of solutions on this branch may be seen in Figure 3. Whereas, at each v, the average energy on branch A is lower than that on the branch of fixed points, the solutions on branch B have higher energies than those of the fixed points.

The branch B solution encountered at $v = v_2$ is a limit cycle with a period of 65.6 days and an amplitude of approximately 500. We could not find solutions that continued this branch to smaller amplitudes for $v > v_2$. In addition, the rate at which the system trajectory converges to the branch B limit cycle slows markedly as v approachs v_2 from below. We conjecture that there is a tangent bifurcation at $v = v_2$ at which the branch of stable limit cycles merges with a branch of lower amplitude, unstable limit cycles, branch C, say. This branch of unstable limit cycles probably bifurcates from the branch of fixed points at a subcritical Hopf bifurcation located at some v_4 where $v_4 < v_2$. This is indicated in the sketch in Figure 5.

In Meacham and Berloff (1997) we show that the steady barotropic circulation has two distinct types of linear instability. One of these can be readily identified with the initial supercritical bifurcation. We conjecture that the second instability is responsible for the later subcritical Hopf bifurcation. These two types of instability differ in how they tap the energy of the basic steady circulation. The primary instability is an instability of the large, stationary meander that lies just to the east of the main recirculation gyre. The second instability is a shear instability of the western boundary current. For basins with a different aspect ratio, the western boundary current instability can be the primary instability. For example, in a basin with four times the meridional extent of the one considered in this paper, it is usually the western boundary current instability that first gives rise to unsteady (limit cycle) solutions. The nature of these instabilities and their dependence on the basin aspect ratio are explored more fully in Meacham and Berloff (1997). A brief description of the primary instability for the basin considered in the current paper is given in Section 5.
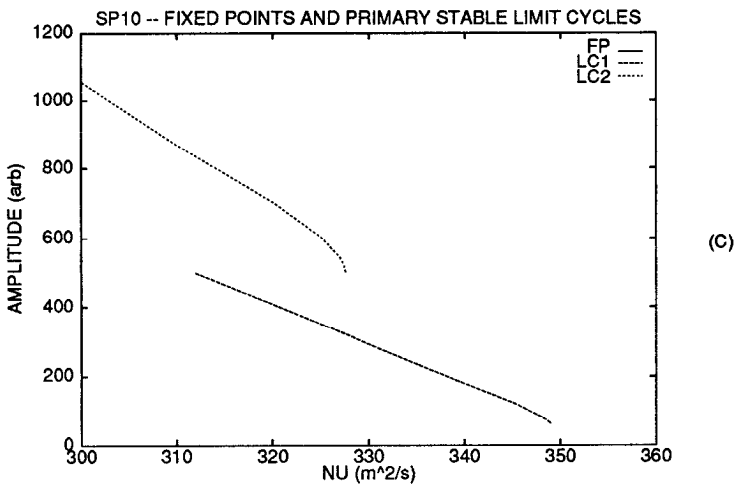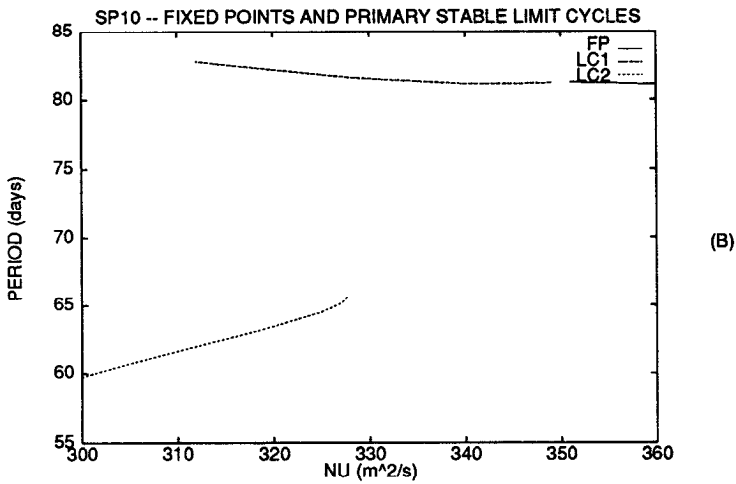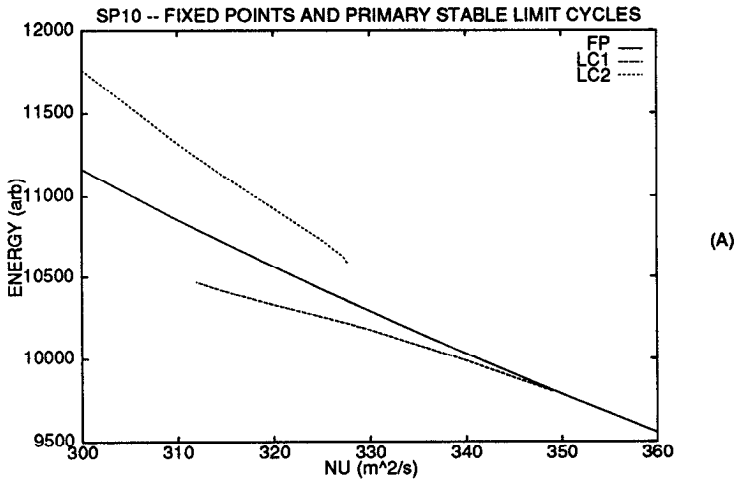
Figure 9. (A) Amplitude, (B) period and (C) energy of the limit cycles on branch A (dashed curve) and those on branch (B) (dotted curve) for $\nu > 300$ m^2 s^{-1}. The energies of the steady states are included in (A) as the solid curve.
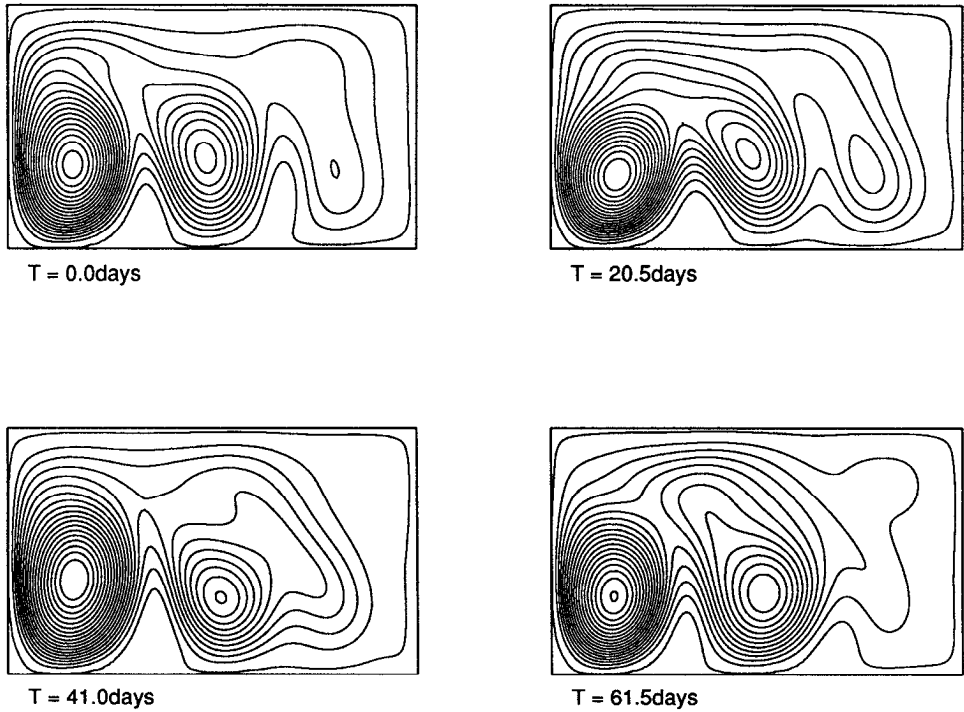
T = 0.0days

T = 20.5days

T = 41.0days

T = 61.5days

Figure 10. Snapshots of the stream function in the basin for various stages during one period of a limit cycle at $\nu = 312$ m^2 s^{-1}. The period of this oscillation is 82.78 days.

c. The continuation of branch A. The average energy of the first family of unsteady solutions, branch A, may be seen in Figure 3. At $\nu = \nu_3$, which lies somewhere between $\nu = 312$ m^2 s^{-1} and $\nu = 310$ m^2 s^{-1}, there is a bifurcation from a limit cycle to a quasi-periodic solution lying on what, in the delay-coordinate phase space, appears to be a two-dimensional torus. Since it is impractical to distinguish between quasi-periodic motion with two fundamental frequencies and an extremely long-period phase-locked limit cycle on a torus, we will refer to both of these as quasi-periodic motion. From the behavior of the rate of convergence to the limit cycle in $\nu > \nu_3$ (as seen in Poincaré sections) as the bifurcation point, ν_3, is approached, this appears to be a supercritical Hopf bifurcation. An example of this toroidal attractor can be seen in Figure 11a ($\nu = 310$ m^2 s^{-1}), a Poincaré section through the attractor may be seen in Figure 11b, while Figure 11c shows the spectrum of a trajectory on this attractor. Close to the bifurcation point, the winding number on the torus is close to 4/3. In the spectrum, one can see two dominant frequency components, one at 0.0760 rad/day and one at 0.1016 rad/day which have a ratio close to 3:4 (about 0.748) (the peak at 0.1520 is presumably a harmonic of the peak at 0.0760). The corresponding periods are 82.7 days and 61.8 days, comparable to the periods of the two families of limit cycles. At lower values of ν, the toroidal attractor gives way to a more

NU=310M^2/S: PHASE SPACE TRAJECTORY

(A)

NU=310M^2/S: POINCARE SECTION (X0=10650)

(B)
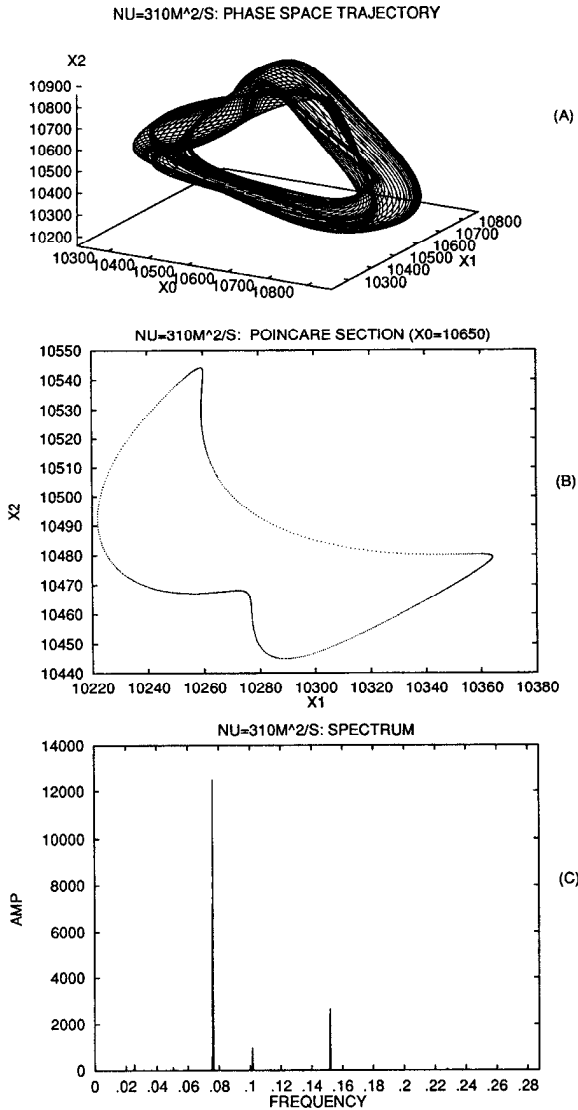
NU=310M^2/S: SPECTRUM

(C)

Figure 11. (A) Segment of a delay coordinate phase space trajectory on, (B) Poincaré section through, and (C) power spectrum of, a toroidal attractor at $v = 310$ m^2 s^{-1}. X0, X1, and X2 are in the arbitrary units of energy we have been using. Frequency on the abscissa of the spectrum is in rad/day.

complicated attractor (Fig. 12a). This has a Poincaré section (Fig. 12b) and power spectrum (Fig. 12c) which suggest that the attractor has become chaotic. Given the finite length of the time series, this conclusion cannot be regarded as a rigorous result.

Below $v = 300$ m^2 s^{-1}, the chaotic attractor appears to lose stability. For example at $v =$

X2   (A)

NU=300M^2/S: POINCARE SECTION (X0=10849.21) (96K DAYS)
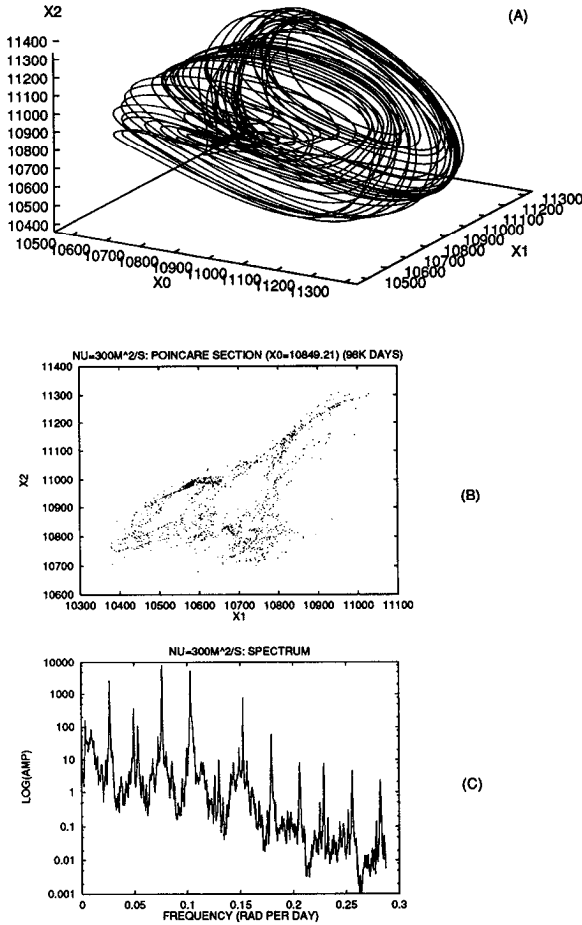

(B)

NU=300M^2/S: SPECTRUM

(C)

Figure 12. (A) Segment of a delay coordinate phase space trajectory on, (B) Poincaré section through, and (C) power spectrum of, an apparently chaotic attractor at $\nu = 300$ m^2 s^{-1}.

298 m^2 s^{-1} and $\nu = 297$ m^2 s^{-1}, a typical trajectory spends a long time in the vicinity of what, from the form of its Poincaré section, appears to be a continuation of the chaotic attractor; however, eventually the trajectory is captured by a stable limit cycle belonging to the second family of unsteady solutions discussed next. It therefore appears likely that near $\nu = 300$ m^2 s^{-1}, there has been a transition from a strange attractor to a hyperbolic strange invariant set.

d. The continuation of branch B. Unlike the A branch, the branch B solutions can be followed easily to low values of the dissipation since some member of this family is attracting at all of the values of ν that we have examined between $\nu = 327.6$ m^2 s^{-1} and $\nu = 100$ m^2 s^{-1}. As noted above, after a tangent bifurcation at $\nu = \nu_2 = 327.6$ m^2 s^{-1}, branch B

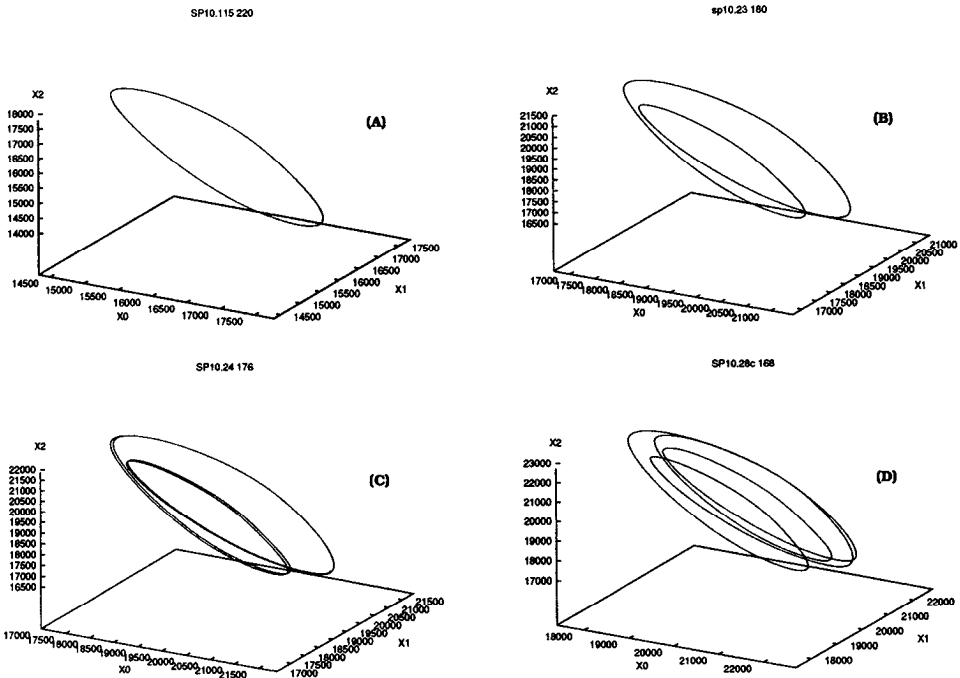SP10.115 220　　　　　　　　　　　　　　　　　　　　sp10.23 180

SP10.24 176　　　　　　　　　　　　　　　　　　　　SP10.28c 168

Figure 13. Delay space trajectories of various limit cycles in the 1:2:4 period doubling sequence. (A) $v = 220$ m^2 s^{-1}, (B) $v = 180$ m^2 s^{-1}, (C) $v = 176$ m^2 s^{-1}, (D) $v = 168$ m^2 s^{-1}.

exists as a set of stable limit cycles until one reaches $v = v_5$, where 281 m^2 s$^{-1} < v_5 < 282$ m^2 s^{-1}. At $v = v_5$ the solution undergoes a pitchfork bifurcation and we see a stable limit cycle with twice the period of its predecessor (114.136 days at $v = 281$ m^2 s^{-1} compared to 57.10 days at $v = 282$ m^2 s^{-1}). For simplicity we will refer to the longer period limit cycle as a period two cycle and its precursor as a period one cycle. Presumably, the period one cycle still exists for $v < v_5$; however, after the bifurcation it will have become an *unstable* period one cycle and we are not able to locate unstable periodic and quasi-periodic attractors. At $v = v_6$, where 258 m^2 s$^{-1} < v_6 < 259$ m^2 s^{-1}, there is a reverse pitchfork bifurcation, and the period two limit cycle collapses onto the period one cycle which regains its stability (see sketch, Fig. 5).

The now stable period one cycle remains the dominant attractor until one reaches $v = v_7$, 210 m^2 s$^{-1} < v_7 <$ m^2 s^{-1}, where there is another pitchfork bifurcation, the period one cycle again loses its stability and another period two orbit appears. This is followed by a third pitchfork bifurcation at $v = v_8$, 176 m^2 s$^{-1} < v_8 < 180$ m^2 s^{-1} at which a stable period four cycle appears. (The actual period of this limit cycle is 204.286 days at $v = 176$ m^2 s^{-1}.) Examples of the period 1, period 2 and period 4 cycles are shown in Figure 13.

The period-doubling sequence does not appear to continue further. Instead, the period four cycle undergoes a Hopf bifurcation at $v = v_9$, 167 m^2 s$^{-1} < v_9 < 168$ m^2 s^{-1}, and a stable toroidal attractor with four loops appears. We encounter a range of v in which the

NU=167M^2/S FRAGMENT OF TRAJ ON T4 ATTRACTOR

NU=167M^2/S: POINCARE SECTION (X0=20178.16)
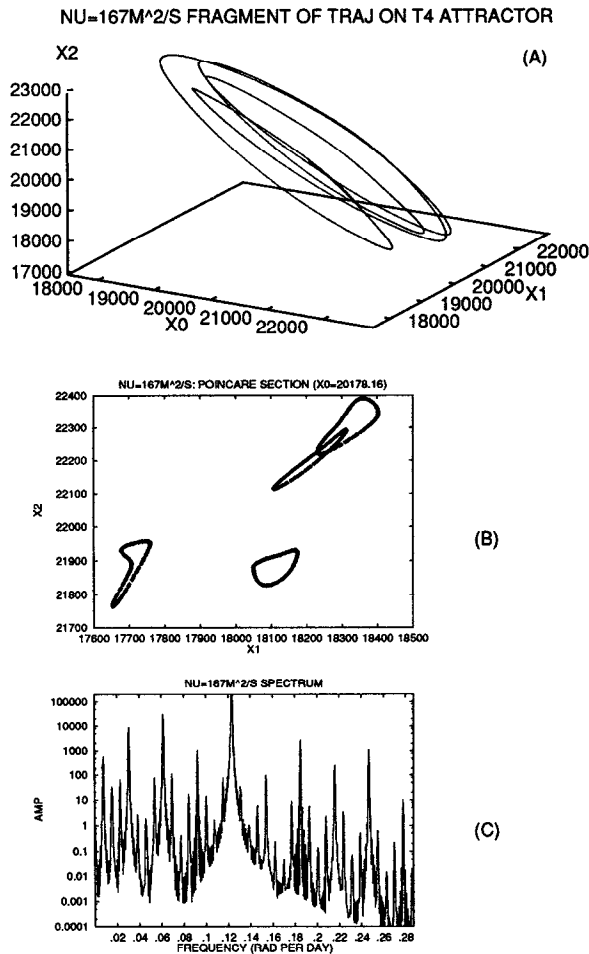

NU=167M^2/S SPECTRUM

Figure 14. (A) Segment of a delay coordinate phase space trajectory on, (B) Poincaré section through, and (C) power spectrum of, a toroidal attractor with four loops at $v = 167$ m^2 s^{-1}.

phase trajectory is attracted to this invariant torus and the motion is, in general, quasi-periodic or a long-period periodic trajectory on the torus. An example is shown in Figure 14 for the case $v = 167$ m^2 s^{-1}. In Figure 14a, part of the trajectory is shown in a 3D perspective plot. The trajectory is tracing over the surface of what is topologically a 2-torus. In Figure 14b, we show a Poincaré section corresponding to the plane $X_0 = 20178.16$ in Figure 14a. The orbit in the Poincaré section is a collection of four simple closed curves, consistent with a two-frequency quasi-periodic motion. This is further suggested by the spectrum of the energy time series (Fig. 14c) which has the form characteristic of two nonlinearly coupled oscillators of incommensurate frequency (c.f. Arnold, 1965). The transition from periodic to two-frequency quasi-periodic behavior is similar to that seen by Brandstater and Swinney (1987) in a study of Taylor-Couette flow.
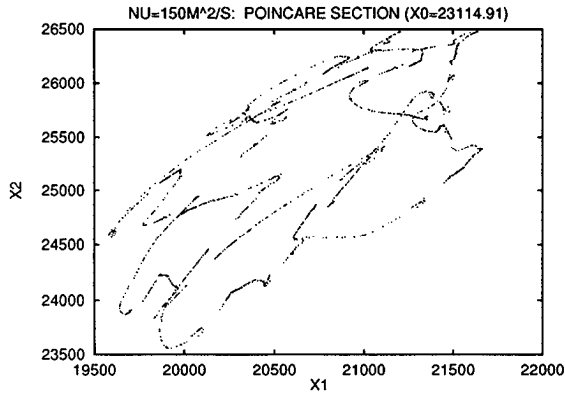
NU=150M^2/S: POINCARE SECTION (X0=23114.91)

Figure 15. Poincaré section through an attractor at $\nu = 150$ m^2 s^{-1}. This appears to be a convoluted 2-torus.

From the theory of nonlinearly coupled oscillators (Arnold, 1965), one anticipates that within the quasi-periodic range there may be intervals in parameter space in which the attractor becomes a periodic orbit on the surface of the torus corresponding to phase-locking of the underlying oscillators, examples of "Arnold tongues." The interleaving of quasi-periodic attractors and intervals of periodic orbits on a torus is quite complicated. For simplicity we will refer to either as motion on a toroidal attractor.

A torus appears be the general form of the attractor down to at least $\nu = 150$ m^2 s^{-1}. At $\nu = \nu_{10}$, 147 m^2 s$^{-1} < \nu_{10} < 150$ m^2 s^{-1}, the toroidal attractor appears to lose stability to an attractor of fractional dimension. Within the range $\nu_{10} < \nu < \nu_9$, as ν decreases, the cross-section of the torus expands and the Poincaré section looks a little more convoluted, e.g. Figure 15 which shows the Poincaré section for $\nu = 150$ m^2 s^{-1}. It is likely that there are other bifurcations in this range that we have failed to resolve. For example, at $\nu = 160$ m^2 s^{-1}, we observe a period 18 torus! Its Poincaré section is shown in Figure 16. Our tentative explanation for this is that, starting with the primary period-4 torus shown in Figure 16, as ν decreased, phase-locking occurred on this torus and a period 18 orbit temporarily became the dominant attractor. However, this period 18 orbit undergoes a secondary Hopf bifurcation (possibly subcritical) to a period 18 torus. Such a phenomenon is unlikely to be structurally stable so we will not dwell on this further. However, for this particular model, the period 18 torus is robust in the sense that the Poincaré section at $\nu = 160.1$ m^2 s^{-1} looks just like the one at $\nu = 160$ m^2 s^{-1}.

Between $\nu = 150$ m^2 s^{-1} and 147 m^2 s^{-1}, there is a bifurcation to what appears, from its Poincaré section, to be a chaotic attractor, an example of which, at $\nu = 147$ m^2 s^{-1}, may be seen in Figure 17a. This Poincaré section was obtained by integrating the numerical model for about 3000 years. In Figure 17b, we show a magnification of the region indicated by a box in Figure 17a. In this, signs of a fractal foliate structure, similar to that of the Hénon attractor, appears to be visible. Part of the power spectrum of an orbit on this attractor is shown in Figure 17c. At low frequencies, one can see the appearance of the broad-band
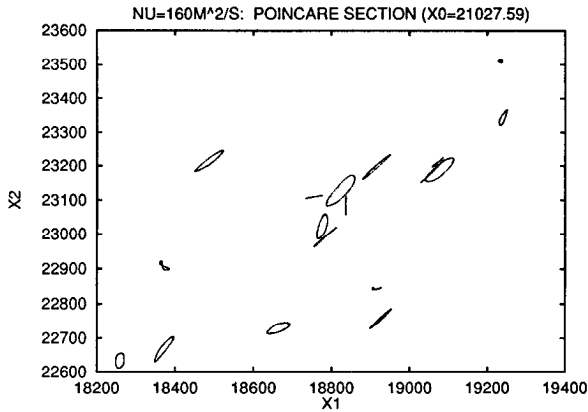
Figure 16. Poincaré section through a toroidal attractor with 18 loops at $\nu = 160$ m^2 s^{-1}.

signal that one expects of motion on a strange attractor. Using the technique of Badii and Politi (1985), as implemented in the numerical package **nn** written by Eric Kostelich (kostelich@asu.edu), we estimated a fractal dimension for the attractor on the Poincaré section and obtained, 1.3 ± 0.1. Taking into account the direction normal to the Poincaré section, it seems that at $\nu = 147$ m^2 s^{-1}, the dominant attractor is a strange attractor with a fractal dimension of roughly 2.3.

The majority of attracting solutions seen at lower values of ν are chaotic and, from their energy values, appear to be continuations of this family. (A narrow band of periodic solutions, first of period 10 and then period 5, was also seen in this range, and there ought to be other periodic windows that we have failed to detect.) As ν decreases, the chaotic attractor expands and its structure becomes less distinct in the delay space projection. (Because of the length of time required to integrate the ocean model, the number of points that we can generate on a Poincaré section is limited.) When a trajectory on the attractor is viewed in a three-dimensional delay coordinate space, this expansion is predominantly in the direction transverse to the plane of the dominant oscillations—the loops of the trajectory that resemble the period 1 limit cycles on branch B. Coincident with this expansion in phase space there seems to be an increase in the dimension of the chaotic attractor. At $\nu = 142$, we estimate the fractal dimension of the chaotic attractor to be 2.7 ± 0.1 while at $\nu = 130$ it is 3.8 ± 0.2.

As ν decreases, the power in the broad-band signal at low frequencies gradually increases (see Fig. 18). It is significant that the "new" frequencies that appear with the bifurcation to a chaotic attractor, i.e. those associated with the appearance of broad-band noise, are low frequencies with periods from one to several years (see Figs. 17c and 18 and note that an annual period corresponds to a frequency of 0.0172). Even a relatively small ocean basin with no seasonal cycle has natural intrinsic time scales of interannual, decadal and centennial periods. Figure 18 suggests that interannual and longer periods become increasingly important as one moves further into the supercritical range. We also note the

NU=147M^2/S: POINCARE SECTION (X0=23708.61)

(A)

NU=147M^2/S: SPECTRUM

(B)

(C)
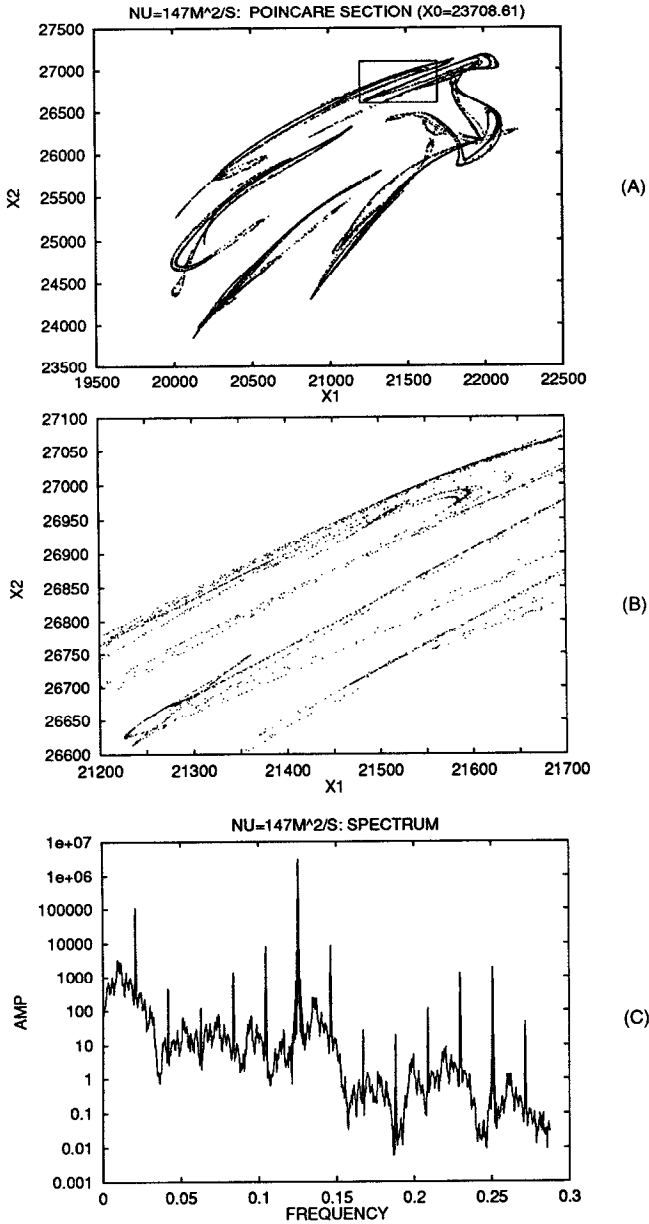
Figure 17. Poincaré section through, and power spectrum of, a chaotic attractor at $\nu = 147 \, m^2 \, s^{-1}$. (A) shows the complete Poincaré section, (B) is a magnification of the area outlined by the box in (A), and (C) shows the power spectrum.
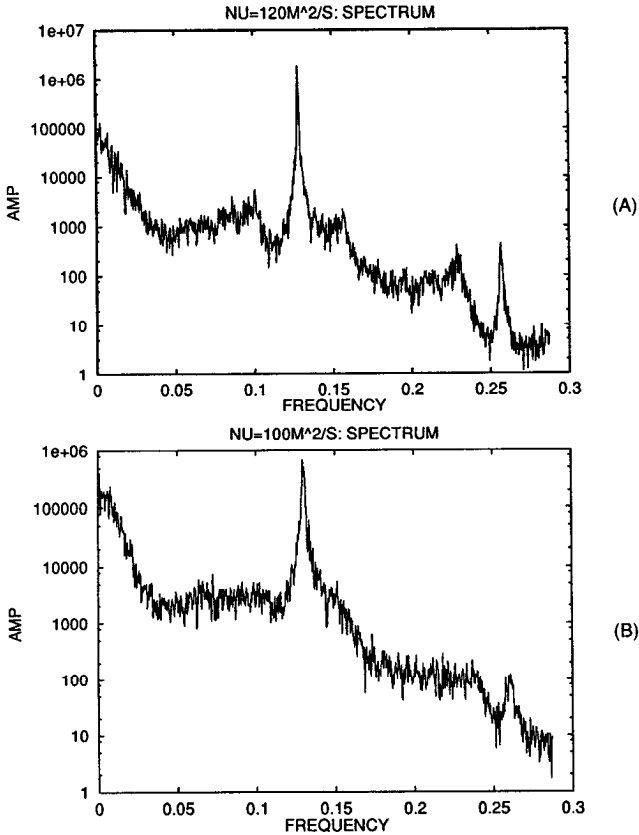
Figure 18. Power spectra of trajectories on apparently chaotic attractors at (A) $v = 120$ m^2 s^{-1}, (B) $v = 100$ m^2 s^{-1}.

persistence of the spectral peak at a period comparable to that of the initial limit cycle that started this family of time-dependent solutions. We conclude that, even far into the supercritical range, the physical mechanism responsible for the initial linear instability that presumably gave rise to this branch continues to exert a strong influence on the now highly time-dependent flow.

e. Resolution. In view of the thinness of the regions of strong dissipation in Figure 19, and the important role dissipation plays in determining the net energy of structures such as fixed points and limit cycles, by balancing the energy put in by wind, we anticipate some dependence on model resolution. At $v = 300$ m^2 s^{-1}, the scale width of a Munk frictional boundary layer is $(v/\beta)^{1/3} = 24.7$ km. For the 8 km resolution used in this model, this corresponds to about three grid intervals. In Figure 19, the strong dissipation seen near the western and southern boundaries seems to be concentrated in a region even narrower than this. One might worry that some of the results above are a consequence of the width of the
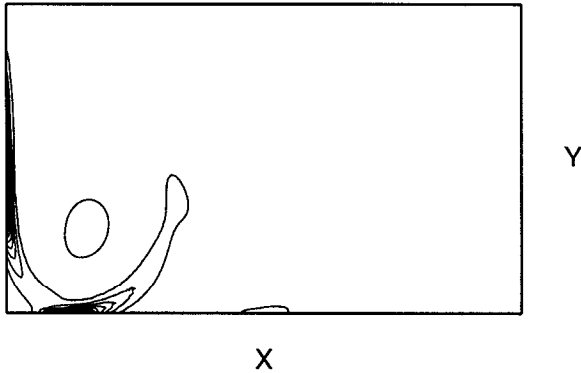
NU=400M^2/S: DISSIPATION

Figure 19. Plot of spatial distribution of frictional dissipation for the steady state at $v = 400$ m^2 s^{-1}. The contour interval is 6.8% of the dissipation maximum and the lowest contour is 3.4% of the maximum. The 3.4% contour is the outer contour spanning both major dissipation zones, together with the isolated closed contour in the middle of the southwestern recirculation gyre.

dissipation zone decreasing, as v is decreased, to the point where it becomes poorly resolved. One can test this by making runs at higher resolution. The point at which the width of the dissipation zones becomes comparable to the grid interval is then postponed to lower values of v. A bifurcation that is caused artificially by the dissipation zone width approaching that of mesh elements would then be expected to occur at lower values of viscosity. We tried to test this for the primary bifurcation by making a number of runs using 4 km resolution (a model with 257 × 129 grid points). Instead of moving to a lower value of v, the primary bifurcation occurred at a slightly higher value of v, somewhere between $v = 360$ m^2 s^{-1} and $v = 370$ m^2 s^{-1}. For a given value of v in the range where both resolutions yield a stable fixed point, the energy of the solution is greater in the higher resolution run. For example, at $v = 400$ m^2 s^{-1}, the energy of the fixed point for the 129 × 65 model is 8749.386 while for the 257 × 129 model it is 8910.66, about 2% higher. (With a 513 × 257 model, at 2 km grid resolution, the energy of this fixed point was 8951.20, less than 0.5% higher than the 4 km case.) Similar small differences may be seen at a value of v at which both resolutions yield limit cycles. For example, at $v = 250$ m^2 s^{-1}, the average energy of the limit cycle for the 129 × 65 model is 14143.53 and the period is 52.35 days while for the 257 × 129 model they are 14861.31 and 51.95 respectively, a difference of about 5% in average energy and less than 1% in period. This suggests that by inadequately resolving the narrow regions of high dissipation, the lower resolution model overestimates the total dissipation, causing the system to equilibrate at a slightly lower energy level. However, in the higher resolution runs we still see a pair of supercritical and subcritical primary bifurcations similar to those seen in the lower resolution runs. The period of the supercritically bifurcating mode near the bifurcation point is slightly longer, being

approximately 81.42 days for the 257 × 129 model at $\nu = 360$ m^2 s^{-1} c.f. about 81.22 days for the 129 × 65 model at $\nu = 350$ m^2 s^{-1}.

The higher resolution model is too expensive to use for long chaotic runs; however, we did make some runs to check that period doubling did occur in the same sequence in the 4 km resolution model as it did in the 8 km resolution model. The comparison may be seen in Figure 20 which shows the periods of periodic solutions found for 160 m^{2}s$^{-1} < \nu < 360$ m^2 s^{-1} for the 8 km case (Fig. 20a) and 4 km case (Fig. 20b). (The points assigned "zero" frequency near $\nu = 160$ m^{2}s^{-1} in both figures are toroidal attractors.)

5. The primary instability

As we have seen, there is an initial Hopf bifurcation near $\nu = 350$ m^2 s^{-1}. In Meacham and Berloff (1997), we show that the steady circulations that result in a barotropic model driven by a steady wind stress of uniform curl have at least two modes of instability. One is an instability of the western boundary layer and is the same as that examined by Ierley and Young (1991). The second has its seat in the flow near the southern zonal boundary where fluid from the western boundary current rejoins the interior circulation. This part of the flow contains several structural units including a predominantly inertial recirculation gyre in the southwestern corner and a strong meander of the southern boundary current just to the east of the recirculation gyre. The second instability involves a strong cyclic exchange of energy between the perturbation and the basic steady flow in the vicinity of this meander.

As an example, we look at the fastest growing linear mode of an unstable steady state, the case $\nu = 349$ m^2 s^{-1}. The fastest growing linear mode is found by an iterative technique. Details can be found in Meacham and Berloff (1997). The eigenvalue (complex frequency) associated with this normal mode is $\omega = a + \iota b$ with $a \approx 0.077$ rad/day and $b \approx 0.00033$ day^{-1}. Several snapshots of this mode corresponding to different phases of its period are shown in Figure 21. The following description is written with the advantage of having watched the evolution of the mode (near limit cycle) as an animation loop. One aspect of this small amplitude time-dependent perturbation is the westward propagation of a wave-like disturbance with a zonal wavelength of about half the basin width. In the eastern half of the basin, this appears to have a standing wave structure in the meridional direction with a half-wavelength equal to the meridional extent of the basin. However, two extrema are present in each zonal crest or trough in the eastern half basin. One lies in the northern half and one in the south. In the eastern half of the basin, the ridges and troughs of the time-dependent disturbance are tilted slightly toward a northwest/southeast orientation. The wave amplitudes are small near the eastern boundary (within about 100 km). As the wave propagates westward the southern extremum intensifies and is deflected northward and southward as it interacts with the standing Rossby wave extension of the western boundary current. The first northward deflection occurs as the southern extremum encounters the east side of the standing wave crest that lies just to the east of the main recirculation gyre. This is followed by a rapid deflection as the perturbation wave passes over the standing wave crest. In the southwest corner, as alternating highs and lows of the

PERIODS OF LIMIT CYCLES FOR 8KM RESOLUTION

(A)

PERIODS OF LIMIT CYCLES FOR 4KM RESOLUTION

(B)
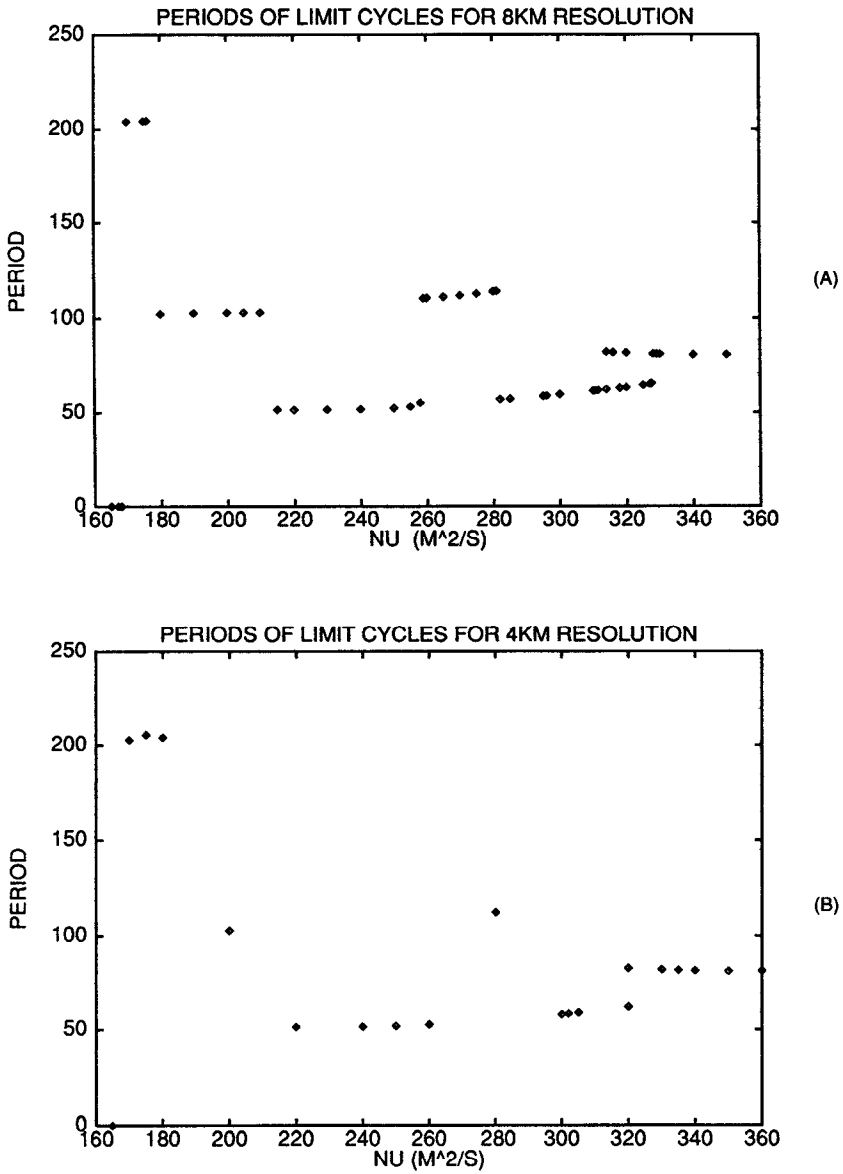
Figure 20. Periods of some of the limit cycles found in the (A) 8 km resolution and (B) 4 km resolution cases.

propagating wave come in along the southern boundary, they are deflected north once more and then rotate cyclonically around the southwestern recirculation—they are advected by the recirculation in the basic state. As they rotate around the recirculation, they weaken. The highs and lows are greatly reduced in strength by the time they have rotated round to

STREAMFUNCTION, CI= .20

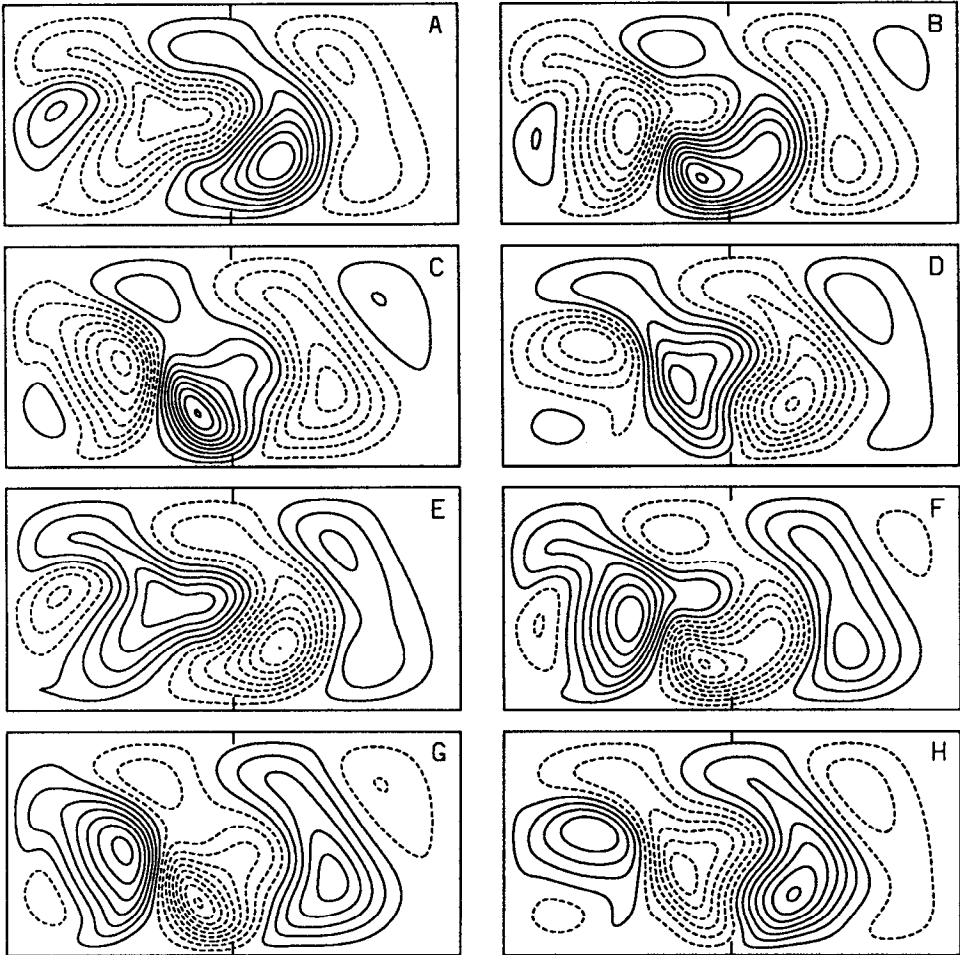Figure 21. Snapshots taken from one period of the slowly growing unstable normal mode of the steady-state circulation at $\nu = 349 \text{ m}^2 \text{s}^{-1}$. The time interval between panels is 10.125 days. Negative contours are dashed. The contour interval is roughly 6% of the difference between maximum and minimum values over a whole period.

the southwest side of the recirculation. The timing of the oscillation appears to be such that a high or low is going around the northeast side of the recirculation just as the remnant of the preceding low or high is diametrically opposite it on the southwest side.

We look further at the nature of the bifurcating mode by examining its energetics. For disturbances close to a steady equilibrium, we decompose the fields:

$$u = \overline{u}(x, y) + u'(x, y, t), \qquad p = \overline{p} + p'$$

where $\bar{u}$ and $\bar{p}$ represent the steady, but spatially varying, equilibrium (the basic state) while u' and p' denote small time-dependent perturbations from this. Substituting this decomposition into (1) yields equations for the perturbations:

$$u'_t + \bar{u} \cdot \nabla u' + u' \cdot \nabla \bar{u} - f k \wedge u' = -\nabla p' + \nu \nabla^2 u'$$

$$\nabla \cdot u' = 0.$$

Taking the dot product of the momentum equation with u', we obtain an energy equation

$$\partial_t K + \nabla \cdot M = F$$

where

$$F = -u'_i u'_j \frac{\partial \bar{u}_i}{\partial x_j} - \nu \frac{\partial u'_i}{\partial x_j} \frac{\partial u'_i}{\partial x_j}$$

$$M = \bar{u} \frac{1}{2} |u'|^2 + p' u' - \nu \nabla K \tag{5}$$

$$\text{and} \quad K = \frac{1}{2} |u'|^2.$$

F represents exchanges of energy between the perturbation and the mean flow (the first term) and dissipation of perturbation energy. M summarizes processes that transport energy from place to place in the perturbation field. F and M are not unique, for example, an alternative form is

$$\hat{F} = \bar{u}_i \partial_{x_j} (u'_i u'_j) - \nu \frac{\partial u'_i}{\partial x_j} \frac{\partial u'_i}{\partial x_j}$$

$$\hat{M} = \bar{u} \frac{1}{2} |u'|^2 + p' u' - \nu \nabla K + \bar{u}_i u'_i u'_j. \tag{6}$$

We looked at the spatio-temporal structure of (6) but it is similar to that of (5) so we will limit our discussion to (5). Figure 22a,b show plots of $u'_i u'_j \, \partial \bar{u}_i / \partial x_j$ and $-\nabla \cdot M$ from one cycle of the slowly growing unstable mode close to the bifurcation point.

In absolute value, the exchange term,

$$P = -u'_i u'_j \frac{\partial \bar{u}_i}{\partial x_j}$$

dominates the dissipative term,

$$D = -\nu \frac{\partial u'_i}{\partial x_j} \frac{\partial u'_i}{\partial x_j}.$$

almost everywhere. In two small regions, the magnitude of the dissipation is of a similar order as the maximum of the production term. All of the terms are almost periodic with a
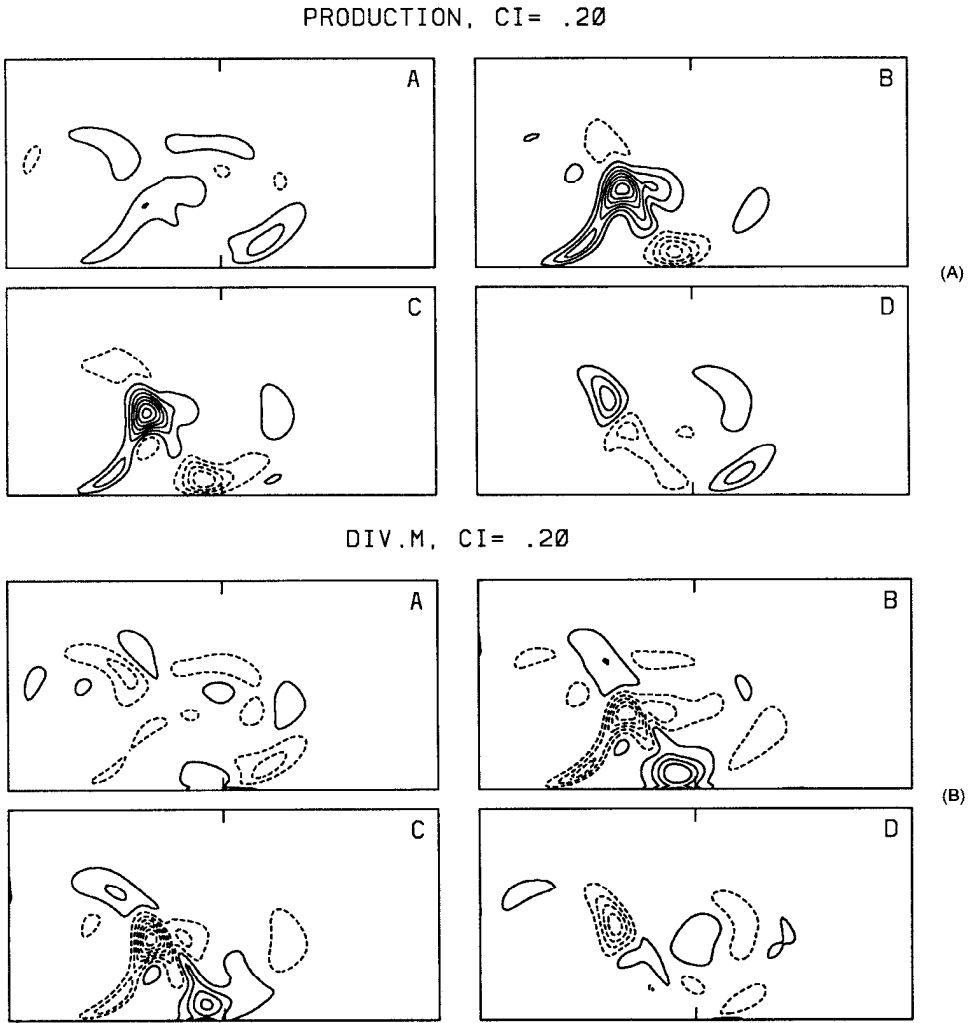
PRODUCTION, CI= .20

(A)

DIV.M, CI= .20

(B)

Figure 22. Snapshots of the main terms in the perturbation kinetic energy equation $\partial_t K = P + D - \nabla \cdot M$ taken from one half-period of oscillation of the slowly growing unstable normal mode of the steady state circulation at $\nu = 349 \ m^2 \ s^{-1}$. The time interval between panels is 10.125 days. Negative contours are dashed. The contour interval is roughly 8% of the difference between maximum and minimum values over a whole period. (A) Production by barotropic energy conversion P, (B) the convergence of the energy fluxes, $-\nabla \cdot M$.

frequency twice that of the bifurcating mode. (M, K, F, P, D are all quadratic in the perturbation and the perturbation is almost linear.) Exchanges are concentrated along the eastern side of the first (westernmost) crest of the standing Rossby wave in the steady state. The direction is from the basic state to the perturbation (positive) near the crest and in the

opposite sense near the trough immediately to the east of the first crest. The structure of $-\nabla \cdot M$ (Fig. 22b) is very similar but of opposite sign showing that most of this energy exchange goes not to or from K' but is transported by M between the maximum and minimum of P. Some can be transported to the boundaries of the domain but the high degree of cancellation between F and $-\nabla \cdot M$ suggests that this is small. In addition, the term $\nu \nabla K'$ is small everywhere compared to P and D. Both the production and flux terms are minimal along the western boundary, strongly suggesting that this instability is not an instability of the western boundary current. Nor is there much energy conversion in the strong southern part of the main recirculation. The strongest values of P occur in neither the western boundary current, the southwestern recirculation, nor the eastern part of the basin, where the perturbation looks most wave-like. We therefore conjecture that the instability is not an instability of the western boundary current or of the recirculation gyre, in the sense that it is not an instability of the boundary current or gyre considered as isolated entities. Nor do we believe that it is a "destabilized" mode of oscillation of the resting basin. (The more wave-like part of the perturbation east of the recirculation zone does not exhibit nodal lines and if wavenumbers inferred from the ridges and troughs in the eastern half of the basin are substituted in the free Rossby wave dispersion relation, the predicted group velocity is eastward.) We are left with the hypothesis that the instability is associated with the large southern meander.

6. Discussion

The model used in this work is clearly not a realistic representation of any real ocean, lacking as it does such things as baroclinicity, topography and a realistic representation of friction. Nevertheless, it demonstrates at least two important points. The first is that even a rather "large" system, a PDE with two spatial and one temporal dimensions in this case, can exhibit behavior that is spatio-temporally complicated, and decidedly nonlinear and yet still be controlled by relatively low-dimensional dynamics. The collapse to such a regime is "natural" because, though the PDE is formally an infinite-dimensional dynamical system, it is dissipative and this strongly damps many of the potential degrees of freedom. For a more formal discussion of this sort of effect in the context of the Navier-Stokes equations, the reader is referred to Robinson (1995), Temam (1995) and Lions *et al.* (1992).

One expects that the dimensions of the attractors in the system will gradually increase as the dissipation is reduced and the results here seem to bear this out. Over the range examined, the attractors have gone from dimension 1 near $\nu = 350 \text{ m}^2 \text{ s}^{-1}$ to a dimension of approximately 4 at $\nu = 130 \text{ m}^2 \text{ s}^{-1}$. If one extrapolated this trend to infinite Reynolds number then one expects that the attractor dimension would also be either huge or infinite. However, many of these additional degrees of freedom ought to be associated with the very small-scale dynamics that constitute "mixing" from the point of view of large-scale motion. There is a limit to the Reynolds number that can be obtained in a numerical model, a limit that is many orders of magnitude lower than in the real ocean. Yet many oceanographers believe that the results of the best modern high resolution ocean simula-

tions bear a reasonable resemblance to the ocean. Since all numerical models are finite-dimensional representations of ocean dynamics, such a belief represents a tacit acceptance by modelers that the ocean can be approximated by a finite dimensional system. This belief is also implicitly held by oceanographers in their observational work which rests upon the assumption that a finite set of measurements allows one to approximate the large scale and mesoscale flow field. From the present work and similar studies of ocean models, we are led to the strong conjecture that at the Reynolds numbers at which they operate, numerical models exhibit low-dimensional dynamics in that the dimension of the underlying attractors is small compared to the explicit dimension of the numerical models (the latter is $O(8000)$ for the current model). This is an unproven conjecture because it is not presently practical to measure the dimension of an attractor buried in an ocean GCM if the dimension of that attractor is $O(10)$ or more, and the trend noted above suggests that by the time one decreased the eddy viscosity to, say, 10 m^2 s^{-1} in the present model, the attractor dimension ought to be outside the range we can measure. (However, it would also be inconsistent to use such a low value of friction in the present model since the physical dissipative scales would then be below the resolution of the model.)

If this conjecture is true, there is still a question of the use to which it may be put. Suppose that the dominant attractor in a GCM has a dimension of between 20 and 21, then Whitney's theorems (Whitney, 1936) show that, in principle, it is possible to construct a dynamical system with dimension 43 that reproduces the dynamics. Further research may eventually provide an answer to how we construct such a system, but the amount of information required to constrain the unknown parameters in such a model may be impractically large. In addition, it may be an even more difficult task to construct a family of low-dimensional models that depend on a physical parameter, for example: the overall strength of the wind-stress curl, in such a way that their attractors change in response to that parameter in the same way as the attractors of the full GCM. Yet we already know a method for constructing a finite-dimensional system that approximates the attractors of the physical system, in ways that we find useful, and at the same time requires that we supply only a few pieces of information beyond the details of the forcing—we discretize the equations of motion and construct a GCM. Perhaps it is possible to trade dimension for the information that is needed to constrain the model; by using a looser embedding with dimension higher than 43 in the example above we may be able to reduce the amount of data needed to constrain the parameters in the model, yet by taking advantage of some of the structure of the low-dimensional attractors, we may be able to construct models with a lower dimension than that of a full GCM, a more efficient representation of the physics.

The second important point is that numerical ocean models, which frequently do use rather simple parameterizations of subgrid scale motion and which tend to be operated in regimes in which the magnitude of the friction is comparable to that used here, can be expected to often be in a low-dimensional regime. This is particularly true of ocean models used in coupled climate models and the climate model itself which is typically strongly damped, ought to have a similar regime. Evidence of low-dimensional behavior can be

seen in equivalent barotropic models (Berloff and Meacham, 1997a) and shallow water models (Speich *et al.,* 1995). Since similar results have been observed in a two-layer ocean model (Berloff and Meacham, 1997b) the conclusion that numerical models are strongly influenced by low-dimensional dynamics is not necessarily vitiated by the addition of extra physics. However, this tendency to approach a state in which only relatively few degrees of freedom are dynamically active might be difficult to see because: (a) it is quite difficult to recognize low-dimensional dynamics when the dimension of the attractor is greater than roughly 3, (b) starting from an arbitrary initial condition, one must wait a considerable period of time for the damped degrees of freedom to damp significantly, (c) a more realistic ocean model is often forced by time-dependent inputs such as surface heating and wind stress, (d) it is not clear what will be the effect of discrete processes such as the "convective adjustment" used in some models. When the model has time-dependent inputs, it is interesting to speculate on the resulting effect on the dynamics. We would guess that the result is to expand the number of active degrees of freedom, for the following reason. Typical monthly or seasonal forcing contains time scales shorter than those required for the ocean model to converge to the attractor that would be the asymptotic limit were the forcing steady. Some of the damped degrees of freedom must therefore have time scales longer than seasonal (and possibly longer than decadal). Presumably these degrees of freedom will be continually forced by the time-dependent inputs and remain active, increasing the effective dimension of the asymptotic dynamics. At the same time many other degrees of freedom ought still to be damped so that it is likely that far fewer degrees of freedom than the total number available are important for the dynamics. The question then becomes to what extent does nonlinearity enable the presence of these additional degrees of freedom to modify the dynamics of those degrees of freedom active during motion on the attractors of the steadily forced system. It will be important to try and extend investigations such as this to problems that include time dependent forcing, for example, by including a seasonal cycle. We are presently embarking upon this. It should be noted that a *periodically* forced model is a simple extension of a steadily forced model. The forcing can be dealt with by defining an extra degree of freedom that is not frictionally damped and is not modified by nonlinear interactions with the remaining degrees of freedom. The generic types of behavior that such a model can possess are then similar to those of steadily forced models except that the attractor in the highly dissipative limit is no longer a fixed point but a limit cycle.

A remarkable result of the present work is the presence of very low frequency variability in this simple, steadily forced GCM. The plateau that can be seen at the low frequency end of the power spectra in Figure 18 extends to extremely long periods—to approximately 180 years when $v = 120 \text{ m}^2 \text{ s}^{-1}$. The appearance of power at the low frequency end of the spectrum can be traced to the bifurcation to a chaotic attractor. Looking at the spectrum in Figure 17, one sees that the broad-band noise that appears with the bifurcation to a chaotic attractor occurs predominantly at relatively long time scales—from one to several years. As the dissipation is further decreased there is a progressive increase in low frequency

variability (Fig. 18). Because the low frequency variability is associated with motion on a strange attractor, long time scale fluctuations in this model are inherently unpredictable. The appearance of powerful, unpredictable, decadal to centennial time scale fluctuations in a relatively simple GCM, if symptomatic of more realistic GCMs and climate models, complicates the task of climate prediction.

Given the importance of understanding the origin of such time scales when trying to unravel the dynamics of climate, it would seem a worthwhile, though not necessarily simple, endeavor to try and unscramble the mechanism responsible for the appearance of such time scales at the bifurcation from a torus to a chaotic attractor. One possible explanation might be that the bifurcation involved is a homoclinic bifurcation of some sort. Trajectories on the attractor might then linger recurrently in the vicinity of a hyperbolic invariant set such as a hyperbolic fixed point or limit cycle. At least one such unstable fixed point and two such unstable limit cycles resulted from the various earlier bifurcations. If these continued down to lower values of ν, one of them may be involved in a homoclinic bifurcation from the torus. Constructing an algorithm to track unstable limit cycles is a significant research problem for a system this large but such an effort would be useful if it helped one understand the origin of low frequency variability.

The majority of the bifurcations that we have described are local (the nature of the transition to the chaotic attractor is unresolved). The structure of the flow field is therefore continuous across the bifurcations. Where the bifurcations are subcritical, as in the case of the transition to limit cycles on the B branch of solutions, there is a finite change in structure going from the steady state to the limit cycle. The limit cycles resemble finite amplitude versions of the streamfunction patterns seen in the linear instabilities, c.f. Figure 21. At first, as ν is reduced, the length scales of the recirculation gyres gradually decrease. However, at still lower ν, the flow becomes dominated by very strong, highly time-dependent large recirculations. Without baroclinic instability, the production of small scale features is inefficient. In this single gyre model, in which vorticity input by the wind has only a single sign, the inability to effectively produce small scale features that can efficiently transfer vorticity to the boundaries means that strong large scale flows are required before the vorticity gradients near the boundaries are sufficient to remove the vorticity pumped in by the wind stress. This is akin to the inertial runaway seen in some steady solutions of wind-driven circulation problems. Several snapshots of the streamfunction in the strongly irregular regime seen at low viscosity ($\nu = 100 \text{ m}^2 \text{ s}^{-1}$) are shown in Figure 23. Despite the irregularity, there is still a significant oscillatory component.

We make some rather tentative conjectures designed to offer a rationalization of some of the results described in Section 4. The way in which some at least of the many degrees of freedom present in this system contribute to the dynamics of the system appears to be as oscillators coupled together by the nonlinearity of the system (the advection terms). These oscillators we identify with the limit cycles seen at the high ν end of the A and B families of time-dependent solutions. We guess that these can be traced to the two types of instabilities identified in the barotropic model by Meacham and Berloff (1997). (We cannot prove this
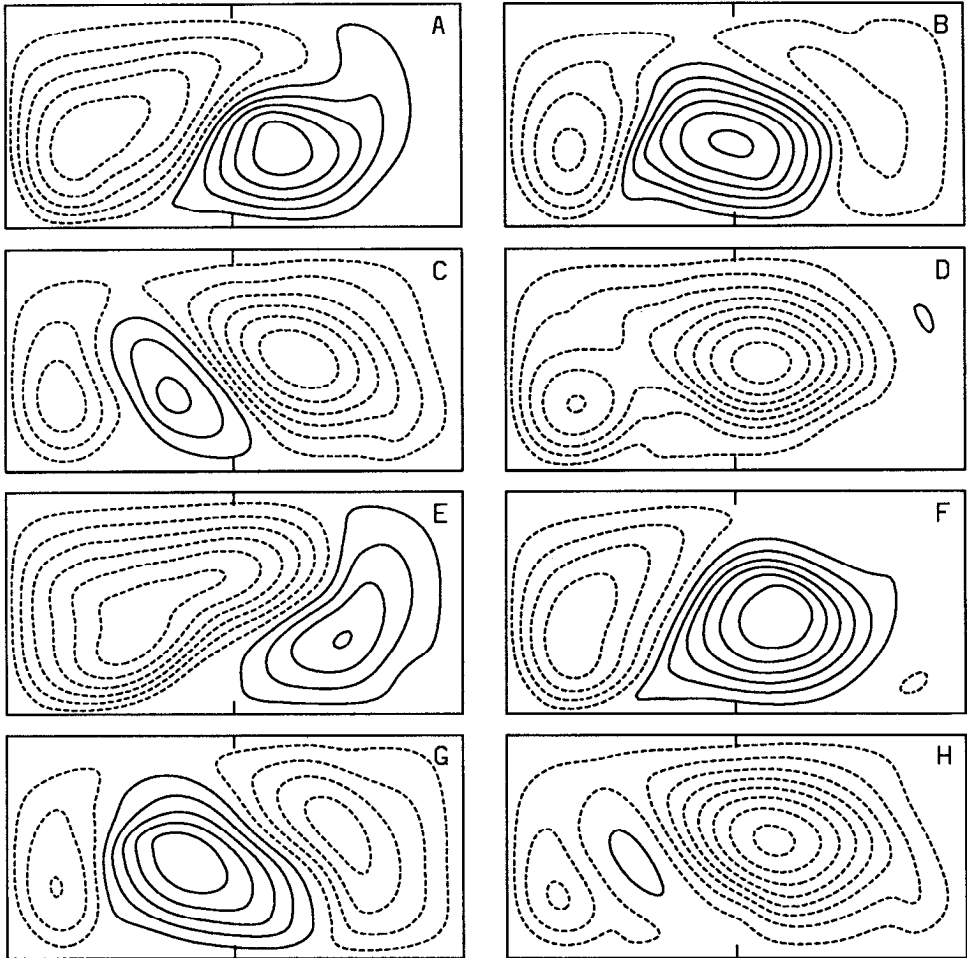
STREAMFUNCTION, CI=10^4

Figure 23. Snapshots of the stream function of the aperiodic flow seen when $v = 100$ m^2 s^{-1}. The interval between images is 10.125 days. Negative contours are dashed. The contour interval is roughly 7% of the difference between the maximum and minimum values over the total time shown.

because we have not been able to follow family B around the tangent bifurcation onto the unstable branch.) For most of a considerable range of v (350 m^2 s^{-1} to 170 m^2 s^{-1}), only either one or two modes of oscillation dominate and the asymptotic behavior of the system could be approximated by a two-degree of freedom dynamical model. Given the magnitude of the flow speed near the western and southern boundaries (e.g. approx 40 cm s^{-1} for $v = 170$ m^2 s^{-1}) and the consequent degree of nonlinearity in the system, this seems fairly remarkable. We are at present trying to model the dynamics on 2D and 3D Poincaré

sections through the fractal attractor at $\nu = 147$ m^2 s^{-1} with relatively simple two- and three-dimensional maps.

One of the consequences of the bifurcation picture shown by this model is that, for a range of flow parameters, multiple, stable, unsteady equilibria are present. This range includes a region where two different stable limit cycles can exist. By using a different value of δ and crossing the marginal curve along a different path through (ϵ, δ) space is possible to make the tangent bifurcation on the B family of solutions occur at a higher value of ν than the supercritical Hopf bifurcation that begins the A family. Under these conditions, there is a range of ν for which both a stable, steady circulation and a stable limit cycle exist. There the steady state is unstable to finite amplitude perturbations; a large enough disturbance will kick the system over into the basin of attraction of the limit cycle.

A useful extension of this work would be to apply a KL analysis to the flow when the system is on an asymptotic attractor and discover the structure of the principal orthogonal modes.

REFERENCES

Arnold, V. I. 1965. Small denominators, I: Mappings of the circumference onto itself. AMS Transl. Ser. 2, *46*, 213–284.

Badii, R. and A. Politi. 1985. Statistical description of chaotic attractors: the dimension function. J. Stat. Phys., *40*, 725–750.

Berloff, P. S. and S. P. Meacham. 1997a. The dynamics of an equivalent-barotropic model of the wind-driven circulation. J. Mar. Res., *55*, 407–451.

—— 1997b. The dynamics of a simple baroclinic model of the wind-driven circulation. J. Phys. Oceanogr., (submitted).

Brandstater, A., J. Swift, H. L. Swinney, A. Wolf, J. D. Farmer, E. Jen and P. J. Crutchfield. 1983. Low dimensional chaos in a hydrodynamical system. Phys. Rev. Lett., *51*, 1442–1445.

Brandstater, A. and H. L. Swinney. 1987. Strange attractors in weakly turbulent Couette-Taylor flow. Phys. Rev. A, *35*, 2207–2220.

Bryan, K. 1963. A numerical investigation of a nonlinear model of a wind-driven ocean. J. Atmos. Sci., *20*, 594–606.

Cessi, P., R. V. Condie and W. R. Young. 1990. Dissipative dynamics of a western boundary current. J. Mar. Res., *48*, 677–700.

Cessi, P. and G. R. Ierley. 1995. Symmetry-breaking multiple equilibria in quasi-geostrophic wind-driven flows. J. Phys. Oceanogr., *25*, 1196–1205.

Charney, J. G. 1955. The Gulf Stream as an inertial boundary layer. Proc. Nat. Acad. Sci., *41*, 731–740.

Doering, C. R. and J. D. Gibbon. 1995. Applied Analysis of the Navier-Stokes Equations, Cambridge University Press, Cambridge, 223 pp.

Farmer, J. D., E. Ott and J. A. Yorke. 1983. The dimension of chaotic attractors. Physica, *7D*, 153–180.

Fofonoff, N. P. 1954. Steady flow in a frictionless homogeneous ocean. J. Mar. Res., *13*, 254–262.

Journal of Marine Research

Fraser, A. M. and H. L. Swinney. 1986. Independent coordinates for strange attractors from mutual information. Phys. Rev. A, *33,* 1134–1140.

Gollub, J. P. and H. L. Swinney. 1975. Onset of turbulence in a rotating fluid. Phys. Rev. Lett., *35,* 927–930.

Hockney, R. 1970. The potential calculation and some applications. Methods in Comput. Phys., *9,* 136–211.

Holland, W. R. 1978. The role of mesoscale eddies in the general circulation of the ocean:— Numerical experiments using a wind-driven quasi-geostrophic model. J. Phys. Oceanogr., *8,* 363–392.

Hudson, J. L. and J. C. Mankin. 1981. Chaos in the Belousov-Zhabotinskii reaction. J. Chem. Phys., *74,* 6171–6177.

Ierley, G. R. 1987. On the onset of inertial recirculation in barotropic general circulation models. J. Phys. Oceanogr., *17,* 2366–2374.

Ierley, G. R. and V. A. Sheremet. 1995. Multiple solutions and advection-dominated flows in the wind-driven circulation. Part I: Slip. J. Mar. Res., *53,* 703–737.

Ierley, G. and W. Young. 1991. Viscous instabilities in the western boundary layer. J. Phys. Oceanogr., *21,* 1323–1332.

Il'in, A. M. and V. M. Kamenkovich. 1964. The structure of the boundary layer in the two-dimensional theory of oceanic current. Oceanology, *4,* 756–769.

Jiang, S., F.-F. Jin and M. Ghil. 1995. Multiple equilibria, periodic and aperiodic solutions in a wind-driven, double-gyre, shallow-water model. J. Phys. Oceanogr., *25,* 764–786.

Kamenkovich, V. M., V. A. Sheremet, A. R. Pastushkov and S. O. Belotserkovsky. 1995. Analysis of the barotropic model of the subtropical gyre in the ocean for finite Reynolds numbers. Part I. J. Mar. Res., *53,* 959–994.

Kostelich, E. J. and H. L. Swinney. 1986. Practical considerations in estimating dimension from time series data, *in* Chaos and Related Nonlinear Phenomena, I. Procaccia and M. Shapiro, eds., Plenum, New York,

Ledwell, J. R., A. J. Watson and C. S. Law. 1993. Evidence for slow mixing across the pycnocline from an open-ocean tracer-release experiment. Nature, *364,* 701–703.

Libchaber, A., C. Laroche and S. Fauve. 1982. Period doubling cascade in mercury, a quantitative measurement. J. de Physique Lett., *43,* 211–216.

Libchaber, A. and J. Maurer. 1982. A Rayleigh-Benard experiment: helium in a small box, *in* Nonlinear Phenomena at Phase Transitions and Instabilities, T. Riste, ed., 259–286.

Lions, J.-L., R. Temam and S. Wang. 1992. On the equations of the large scale ocean. Nonlinearity, *5,* 1007–1053.

Lorenz, E. N. 1963. Deterministic non-periodic flow. J. Atmos. Sci., *20,* 130–141.

Meacham, S. P. 1997. The response of a small basin circulation to variations in forcing. J. Phys. Oceanogr., (submitted).

Meacham, S. P. and P. S. Berloff. 1997. Instabilities of a steady, barotropic, wind-driven-circulation. J. Mar. Res., (submitted).

Moore, D. W. 1963. Rossby waves in ocean circulation. Deep-Sea Res., *10,* 735–747.

Morgan, G. W. 1956. On the wind-driven ocean circulation. Tellus, *8,* 301–320.

Munk, W. H. 1950. On the wind-driven ocean circulation. J. Meteor., *7,* 79–93.

Munk, W. H., G. Groves and G. F. Carrier. 1950. Note on the dynamics of the Gulf Stream. J. Mar. Res., *9,* 218–238.

Oguz, T., D. G. Aubrey, V. S. Latun, E. Demirov, L. Koveshnikov, V. Diacanu, H. I. Sur, S. Besiktepe, M. Duman, R. Limeburner and V. Eremeev. 1994. Mesoscale circulation and thermohaline structure of the Black Sea observed during HydroBlack'91. Deep-Sea Res., *41,* 603–628.

Oguz, T., V. S. Latun, M. A. Latif, V. V. Vladimirov, H. I. Sur, A. A. Markov, E. Ozsoy, B. B. Kotovshchikov, V. V. Eremeev and U. Unluata. 1993. Circulation in the surface and intermediate layers of the Black Sea. Deep-Sea Res., *40*, 1597–1612.

Oguz, T., P. E. La Violette and U. Unluata. 1992. The upper layer circulation of the Black Sea: Its variability as inferred from hydrographic and satellite observations. J. Geophys. Res., *97*, 12569–12584.

Packard, N. H., J. P. Crutchfield, J. D. Farmer and R. S. Shaw. 1980. Geometry from a time series. Phys. Rev. Lett., *45*, 712–716.

Pedlosky, J. 1987. Geophysical Fluid Dynamics, 2nd ed, Springer-Verlag, New York.

Rhines, P. B. 1975. Waves and turbulence on a beta-plane. J. Fluid Mech., *69*, 417–443.

—— 1979. Geostrophic turbulence. Ann. Rev. Fluid Mech., *11*, 401–441.

Roache, P. J. 1982. Computational Fluid Dynamics, Hermosa, Albuquerque.

Robinson, J. C. 1995. Finite-dimensional behavior in dissipative partial differential equations. Cháos, *5*, 330–345.

Roux, J.-C., R. H. Simoyi and H. L. Swinney. 1983. Observation of a strange attractor. Physica, *8D*, 257–266.

Ruelle, D. and F. Takens. 1971a. On the nature of turbulence. Comm. Math. Phys., *20*, 167–192.

—— 1971b. On the nature of turbulence. Comm. Math. Phys., *23*, 343–344.

—— 1976. A two-dimensional mapping with a strange attractor. Comm. Math. Phys., *50*, 69–77.

Sheremet, V. A., V. M. Kamenkovich and A. R. Pastushkov. 1995. Analysis of the barotropic model of the subtropical gyre in the ocean for finite Reynolds numbers. Part II. J. Mar. Res., *53*, 995–1024.

Simoyi, R. H., A. Wolf and H. L. Swinney. 1982. One-dimensional dynamics in a multicomponent chemical reaction. Phys. Rev. Lett., *49*, 245–248.

Speich, S., H. Dijkstra and M. Ghil. 1995. Successive bifurcations in a shallow-water model applied to the wind-driven ocean circulation. Nonlinear Proc. Geophys., *2*, 241–268.

Stommel, H. 1948. The westward intensification of wind-driven ocean currents. Trans. Am. Geophys. Union, *29*, 202–206.

Takens, F. 1981. Detecting strange attractors in turbulence, *in* Lecture Notes in Mathematics, *898:* Dynamical Systems and Turbulence, D. A. Rand and L.-S. Young, eds. Springer-verlag, 366–381.

Temam, R. 1995. Navier-Stokes Equations and Nonlinear Functional Analysis, 2nd ed., CBMS-NSF regional conference series in applied mathematics, *66.* SIAM, Philadelphia. 141 pp.

Whitney, H. 1936. Differentiable manifolds. Ann. Math., *37*, 645–680.